


ORIGINAL ARTICLE

MBNL-dependent impaired development within the neuromuscular system in myotonic dystrophy type 1

Julie Tahraoui-Bories¹ | Antoine Mérien¹ | Anchel González-Barriga² |
 Jeanne Lainé² | Céline Leteur³ | Hélène Polvèche³ | Alexandre Carteron³ |
 Juliette Duchesne De Lamotte⁴ | Camille Nicoleau⁴ | Jérôme Polentes³ |
 Margot Jarrige³ | Mário Gomes-Pereira² | Erwann Ventre⁵ | Pauline Poydenot⁵ |
 Denis Furling² | Laurent Schaeffer⁶ | Claire Legay⁷ | Cécile Martinat¹ 

¹INSERM/UEVE UMR 861, Université Paris Saclay, I-STEM, Corbeil-Essonnes, France²INSERM, Institut de Myologie, Centre de Recherche en Myologie, Sorbonne Université, Paris, France³CECS/AFM, I-STEM, Corbeil-Essonnes, France⁴IPSEN Innovation, Les Ulis, France⁵CYTOO SA, Minatec, Grenoble, France⁶INMG, INSERM U1217, CNRS UMR5310, Université Lyon 1, Université de Lyon, Hospices Civils de Lyon, Lyon, France⁷CNRS, SPINN—Saint-Pères Paris Institute for the Neurosciences, Université Paris Cité, Paris, France**Correspondence**

Cécile Martinat, PhD, INSERM/UEVE UMR 861, Université Paris Saclay, I-STEM, I-STEM, 28 rue Henri Desbrières 91100 Corbeil-Essonnes, France.
 Email: cmartinat@istem.fr

Funding information

French Muscular Dystrophy Association;
 Association Française contre les Myopathies;
 Agence Nationale de la Recherche

Abstract

Aims: Myotonic dystrophy type I (DM1) is one of the most frequent muscular dystrophies in adults. Although DM1 has long been considered mainly a muscle disorder, growing evidence suggests the involvement of peripheral nerves in the pathogenicity of DM1 raising the question of whether motoneurons (MNs) actively contribute to neuromuscular defects in DM1.

Methods: By using micropatterned 96-well plates as a coculture platform, we generated a functional neuromuscular model combining DM1 and muscleblind protein (MBNL) knock-out human-induced pluripotent stem cells-derived MNs and human healthy skeletal muscle cells.

Results: This approach led to the identification of presynaptic defects which affect the formation or stability of the neuromuscular junction at an early developmental stage. These neuropathological defects could be reproduced by the loss of RNA-binding MBNL proteins, whose loss of function in vivo is associated with muscular defects associated with DM1. These experiments indicate that the functional defects associated with MNs can be directly attributed to MBNL family proteins. Comparative transcriptomic analyses

Abbreviations: AChR, Acetylcholine receptor; BoNT/A, Botulinum neurotoxin type-A; DEGs, Differentially expressed genes; DKO, Double knock-out; DM1, Myotonic dystrophy type 1; DMPK, Myotonic dystrophy associated protein kinase; DSEs, Differentially skipped exons; hESC, Human embryonic stem cells; hiPSCs, Human-induced pluripotent stem cells; hPSCs, Human pluripotent stem cells; ISL1, Islet-1; MBNLs, Muscleblind proteins; MHC, Myosin heavy chain; MNs, Motoneurons; PCA, Principal component analysis; TuJ1, Tubulin β -III.

This is an open access article under the terms of the [Creative Commons Attribution-NonCommercial-NoDerivs](https://creativecommons.org/licenses/by-nc-nd/4.0/) License, which permits use and distribution in any medium, provided the original work is properly cited, the use is non-commercial and no modifications or adaptations are made.

© 2022 The Authors. *Neuropathology and Applied Neurobiology* published by John Wiley & Sons Ltd on behalf of British Neuropathological Society.

also revealed specific neuronal-related processes regulated by these proteins that are commonly misregulated in DM1.

Conclusions: Beyond the application to DM1, our approach to generating a robust and reliable human neuromuscular system should facilitate disease modelling studies and drug screening assays.

KEYWORDS

induced pluripotent stem cells, MBNL proteins, Motoneurons, myotonic dystrophy type 1, neuromuscular junction

INTRODUCTION

Myotonic dystrophy type 1 (DM1) is a dominant hereditary muscular dystrophy which results from the expansion of an unstable CTG repeat in the 3' untranslated region of *Myotonic Dystrophy Associated Protein Kinase (DMPK)* [1, 2]. DM1 is considered the most common adult-onset muscular dystrophy with considerable clinical heterogeneity, mainly characterised by muscle weakness and myotonia and also systemic manifestations involving cognitive impairment, cataracts and cardiac conduction abnormalities [3–5]. A correlation has been observed between the severity of the symptoms and the number of CTG repeats with longer CTG repeat expansions correlating with an earlier age of onset and more severe forms of the disease [6, 7].

In skeletal muscle, the main pathogenic process in DM1 arises from an RNA-mediated mechanism involving the dysfunction of alternative splicing regulator proteins by mutant *DMPK* transcripts which results in inappropriate expression of developmental splice isoforms in adult tissues [8]. One of the most well-described mechanisms at the origin of this misregulation resides in the direct sequestration of proteins from the MBNL family within nuclear aggregates formed by mutant RNAs containing expanded CUG repeats [9, 10]. Dozens of splicing events are thus found to be misregulated in skeletal muscle biopsies from DM1 patients [11]. A couple of these events have been correlated directly with DM1 symptoms, such as the myotonia that characterises DM1, which has been associated with abnormal splicing of the skeletal muscle-specific chloride channel 1 (*CIC-1*) or muscle weakness more recently associated with the defective splicing of *DMD* exon 78 [12–14].

Although DM1 has long been considered to be mainly a muscle disorder, emerging evidence suggests the involvement of peripheral nerves in the pathogenicity of DM1. Several abnormalities involving nerve terminals such as multiple endplates on the same muscle fibre, abnormal endplate size and expanded terminal arborisations have been observed in patients' biopsies [15, 16]. More recently, neurophysiological studies in two different cohorts of DM1 patients reported neuromuscular transmission abnormalities [17, 18]. These observations were confirmed to a certain extent in a severe murine model of DM1 in which abnormalities in the size and complexity of endplates were observed in the diaphragm [19]. However, the mechanisms by which the mutation might affect muscle innervation are not clearly understood. These symptoms can derive from muscle fibre damage, as evidenced in biopsies of clinically affected patients [17].

Key points

- Myotonic dystrophy type I (DM1) human-induced pluripotent stem cell (hiPSC)-derived spinal motoneurons harbour neurite outgrowth defects reproduced by muscleblind proteins (MBNL) depletion.
- Overexpression of MBNL1 protein in DM1 hiPSC-derived spinal motoneurons reverses the abnormal neuritogenesis.
- Defective neuritogenesis of DM1 and MBNL-depleted hiPSC-derived spinal motoneurons contributes anterogradely to abnormal neuromuscular communication.
- MBNL proteins regulate the expression of specific synaptic-related genes that are commonly deregulated in DM1 hiPSC-derived spinal motoneurons.

Nonetheless, peripheral nerve dysfunction might also contribute to these mechanisms.

In this regard, the detection of nuclear mutant RNA aggregates in association with MBNL proteins in motor neurons from postmortem biopsies of DM1 patients raises the possibility, as described for skeletal muscle cells, of a toxic RNA-mediated mechanism within the motoneuronal compartment which may affect the development, function or stability of the neuromuscular junction [20]. Thus, the potential contribution of MBNL proteins to motoneurons and neuromuscular junction defects remains an open question.

To test this hypothesis, we took advantage of the recent progress made in the combination of human pluripotent stem cell technology with advanced tissue culture systems to recapitulate human neuromuscular structure and function [21]. We based our approach both on our recently optimised protocol to rapidly and efficiently convert hiPSCs into a homogenous population of spinal motoneurons (hiPSCs-derived spinal MNs) [22] and on the development of cocultures between hiPSC-spinal MNs and human skeletal muscle cells using micropatterned 96-well plates [23]. Combining skeletal muscle cells with hiPSCs-spinal MNs derived from DM1 patients or depleted for MBNL proteins by CRISPR/Cas9 technology, we investigated the contribution of motoneurons in the neuromuscular defects observed in DM1.

MATERIALS AND METHODS

hiPSC and differentiated cells

Human-induced pluripotent stem cells (hiPSC), the control (CTRL) and the three DM1 (named DM1_1, DM1_2, DM1_3) were generated from skin fibroblasts derived from nonaffected and DM1 affected patients as previously described [24]. The length of the repeat expansion was previously estimated to be approximately 2700 CTG repeats in each DM1 hiPSC line generated by Southern Blot analysis [24]. Briefly, hiPSC were grown on culture dishes-coated vitronectin (Gibco®) and maintained in iPS-Brew XF medium (Miltenyi Biotec®). Cell passaging was performed manually under the binocular loupe; colonies are cut as squares using a needle (Dutscher, 050103B) every 5 days, and the culture medium was changed every 2 days. Knock-out MBNL hiPS cells (*MBNL1(-/-)*, *MBNL2(-/-)* and *MBNL1(-/-); MBNL2(-/-)* - named DKO) were generated from a nonaffected hiPSC line by using CRISPR/Cas9 technology as previously described [24]. CTG-depleted DM1 cell line was developed from a DM1 hiPS cell line (DM1_3) by using CRISPR/Cas9 technology and named DM1_3_ΔCTG [25]. The conversion of hiPSC into spinal motoneurons was performed as previously described [22]. Briefly, hiPSC were dissociated enzymatically using Stem Pro Accutase (ThermoFisher®) for 5 min at 37°C, 5% CO₂ and plated in suspension in 25 cm² flasks (Dutscher®) at 1.5 million per flask in an induced-motoneuronal medium supplemented with cytokines every 2 days. After 14 days of differentiation, embryoid bodies were dissociated and motoneuron phenotype was assessed by immunolabelling for Islet1 (ISL1). Human primary control myoblasts (gift of D. Furling, Institute of Myology, Paris) were cultured in a growth medium (DMEM, FBS 10%, 0.5 ng/ml bFGF and 5 ng/ml EGF) and cryopreserved in a freezing solution (CryoStor, Stem Cell technology®). After two to three cell passages, primary myoblasts were purified on CD56 microbead columns (Miltenyi Biotec®) followed by immunolabelling for Desmin to estimate the percentage of myoblast cells (supporting information Figure S4).

Coculture protocol

The 96 micropatterned-well plates were designed and provided by CYTOO SA [23] (Minatec BHT, Grenoble, France). At D0, myoblasts were seeded at 20,000 cells per well in DMEM-F12 glutamax (ThermoFisher®) supplemented by 20% foetal bovine serum (Sigma-Aldrich®) and 0.1% penicillin/streptomycin (ThermoFisher®) (supporting information Material and Method Table S1). At D2, after two washes with basal medium, the growth medium was replaced by the differentiation medium composed of DMEM-F12 glutamax and 2% horse serum (ThermoFisher®, 26050088). At D4, hiPSC-derived MNs were seeded at 40,000 cells per well in DMEMF12-glutamax, neurobasal medium (Vol:Vol) supplemented with BDNF (Miltenyi Biotec®), GDNF (Miltenyi Biotec®), DAPT (Sigma-Aldrich®) and Y-27632 (Stem Cell®) (supporting information Material and Method Table S1). Cocultures were maintained for at least 7 days.

Immunostaining

Motoneurons derived from hiPSC were fixed with a solution containing 4% paraformaldehyde (PFA-Euromedex®) for 8 min at room temperature. Cocultures were fixed vol:vol with a solution containing 8% paraformaldehyde (PFA-Euromedex®, 15710) for 10 min at room temperature. Primary antibodies were diluted in PBS/1% BSA/0.2% Triton X-100 and incubated overnight at 4°C. Appropriate secondary antibodies were added for 1 h at room temperature in the presence of Hoechst 33258 (ThermoFisher®, H3569). Primary and secondary antibodies are listed in the supporting information Material and Method Table S2.

Fluorescent in situ hybridisation (FISH)

FISH experiments were performed as previously described [26]. Briefly, cells were fixed with PBS buffer containing 4% PFA (Electron Microscopy Science, 20 µl/well) for 20 min at room temperature and washed with 200 µl of PBS. Cells were then incubated overnight at 4°C with 70% Ethanol (60 µl/well). After PBS wash, cells were rehydrated with a solution of PBS containing 5mM MgCl₂ for 15–30 min and then sequentially incubated with prehybridisation buffer (50 mM Phosphate buffer, 40% formamide, 2X SSC, 50 µl/well) for 15–30 min and hybridisation buffer (prehybridisation buffer with 0.2% BSA and 7% Dextran, 50 µl/well) containing 300 ng/ml of the (CAG)₁₀-Cy5 probe (5'Alexa 647-TTCTTATTCTTCAGCAGCAGCAGCAGCAGCAGCAGCAGCAG3') (Operon) overnight at 37°C. The washing steps consisted of prewarmed washing buffer (prehybridisation buffer + 0.2% BSA, 60 µl) for 15 min at RT followed by the addition of washing buffer (80 µl) and incubation for 30 min at 37°C. Cells were washed twice in PBS before nuclei counterstaining Hoechst 33258 (ThermoFisher®, H3569). Plates were stored at 4°C until analysis. Nuclear foci detection was performed using the Cellomics Array Scan VTI high-content imaging system (ThermoFisher®) with the 20X objective. Images were acquired in high-resolution camera mode on two channels, and quantification was performed as previously described [26].

Image acquisition and analysis

Images for hiPSC-derived motoneurons were acquired using ImageXpress micro imaging system (Molecular Devices®) and analysed using MetaXpress for automated quantification following the instructions from the software. The percentage of ISL1 and TUJ1 positive cells, a transcription factor specific for motoneurons and the pan-neuronal class III beta-tubulin, respectively, was automatically determined by counting the number of cells expressing ISL1 or TUJ1 over the total number of cells counterstained with Hoechst, using, for both, the metaXpress software tool 'Find Round Objects' following the instructions from the software (MetaXpress). Neurite length was determined by using the metaXpress tool 'fibres bioapplication module' and normalised to the total number of ISL1-positive cells (supporting information Material and Method 5). Images of the coculture system were acquired using Spinning Disk microscopy (Zeiss®) with the 20X and 40X objectives and a z-stack

plan. For quantification of the AChR clustering, neuritic network and myotube area, each image taken was processed as a maximum projection and analysed by using Fiji Software. The following quantifications were performed semimanually. The total area and mean size of AChR clusters were determined by an algorithm developed in-house in Fiji (supporting information Material and Method 1). The neurite outgrowth was measured by applying an intensity threshold and a background correction to detect the neurites stained by TUJ1, class III beta-Tubulin shown to be expressed in the soma and the neuritic processes of neurons. The number of branches was measured as intersections between neurites from the cluster of soma (supporting information Material and Method 2). Islet1 quantification was determined by automatically counting the number of Islet1-positive cells by micropattern using an intensity threshold on Fiji software. The myotube area was quantified by delimiting the cells stained by MF20 (MHC) antibody and application of an intensity threshold (supporting information Material and Method 3). From day 4 in coculture, visual contractions were recorded in phase contrast using Spinning Disk (Zeiss®) under a controlled atmosphere (37°C, 5% CO₂). Movie acquisition lasted 2 min, and they were analysed using the detection of pixel variations on Fiji Software and then visual contractions were analysed by the kymograph tool.

MBNL1-AAV2 transduction in hiPSC-derived MNs

AAV vectors used in this study, pAAV2[Exp]-EF1A>hMBNL1 [NM_021038.5]:WPRE (functional titre: 2.05×10^{11} GC/ml) and pAAV2 [Exp]-EF1A>EGFP:WPRE (functional titre: 5.66×10^{11} GC/ml) were constructed and packaged by VectorBuilder. The vector IDs, VB211128-1086afy and VB900088-2252axv, respectively, can be used to retrieve detailed information about the vector on vectorbuilder.com. hiPSC-derived MN progenitors were transduced at D10 with AAV2 vectors diluted at 10,000 MOI. The amount of virus needed to achieve this multiplicity of infection (MOI) was based on the cell number per well for each AAV condition. hiPSC-derived MN progenitors were seeded in 96-well plates at 75,000 cells/cm² in N2B27 medium and supplemented with Rock inhibitor at 10 µM as previously described [27, 28]. Five hours after the first transduction, a second infection was performed at the same MOI by adding half of the medium. The medium was changed 24 h after the transduction and twice a week for 20 days. For the analysis, plates were fixed with 8% PFA vol/vol, and immunostainings were performed as previously described in Section 2. Neuritic length, MBNL1 expression and percentage of Islet1-positive cells were quantified using the ImageXpress micro Imaging system (Molecular Devices®) and the bioapplications software following the manufacturer's instructions.

Calcium flux assay

Living cells were incubated in an HBSS^{+/+} solution (supporting information Material and Method Table S1) containing a Cal520 probe (2 µM-Abcam®) at 37°C, 5% CO₂. After 25 min, the cells were washed

twice with an HBSS^{-/-} solution and kept at room temperature for 15 min. The recording was performed using Spinning Disk Microscopy (Zeiss®) in a controlled atmosphere (37°C, 5% CO₂). Basal acquisitions were set at 200 ms intervals, and two different fields were acquired per well. The inhibition of synaptic activity was evaluated after different drug treatments. After a basal acquisition of each field, [1] 100 µM of tubocurarine chloride (Sigma-Aldrich®) was applied to each well and a stream acquisition was performed for 1 min; [2] the recombinant neurotoxin botulinum serotype A, generated by Ipsen® as previously described [29], was added at 5 nM, and acquisitions were performed after 4 and 8 h of treatment. In contrast, the activation of synaptic activity was evaluated after treatment with L-Glutamic acid (100 µM-Sigma-Aldrich®). Placebo experiments were conducted by adding drugs to myotubes alone without hiPSC-derived MNs or by treating cocultures with a buffer solution that did not contain any of the chemical reagents. The calcium flux assay analysis was performed semi-automatically using Fiji Software, and the exported raw data were processed on Microsoft Excel to generate the $\Delta F/F_0$ curve (supporting information Material and Method 4). Briefly, for each condition, two fields per well were analysed. For each field, one ROI (Region of interest) determined by using the ROI manager on Fiji Software has been determined for each micropattern (one ROI was also generated for the background signal to calculate the corrected fluorescence). The Ca²⁺ activity (=ROI) was specifically determined in the myotubes by segmenting one by one each micropattern without considering the cluster of soma and automatically analysed to generate the mean grey intensity value over time. The curve of calcium response is represented as the ratio $\Delta F/F_0$ as previously described [23, 28]. Briefly, this ratio represents $(F - F_0) / F_0$ in which F_0 represents the mean fluorescence of basal values in the untreated condition or before drug treatment, whereas ΔF represents the corrected fluorescence minus the mean fluorescence of basal values.

RNA isolation and RT-qPCR analysis

Total RNAs were isolated using the RNeasy Mini extraction kit (Qiagen®) according to the manufacturer's protocol. RNA levels and quality were checked using the NanoDrop® technology. cDNA was synthesised using SuperScript III (ThermoFisher®). Quantitative polymerase chain reaction (qPCR) analysis was performed using a QuantStudio 12K Flex real-time PCR system (Applied Biosystem®). Primer sequences are detailed in the supporting information Material and Method Table S3. All analyses were performed with at least three technical replicates per plate. The 2^{- $\Delta\Delta$} Ct method was used to determine the relative expression level of each gene. All expression data were normalised to three housekeeping genes (18S, cyclophilinA and GAPDH).

Protein extraction and Western blot analysis

Western blot analyses were performed as previously described [26]. Briefly, cells were lysed in RIPA 1X buffer (Sigma®) containing

protease inhibitors (Sigma[®]) and phosphatase inhibitors (Roche[®]). Proteins were quantified by Pierce BCA Protein Assay kit (Pierce[®]) using a multiplate colourimetric reader, CLARIOstar (BMG Labtech[®]). Protein extracts (20 to 40 µg) were loaded on a 4%–12% SDS-PAGE gradient (NuPage Bis-Tris gels, Invitrogen[®]) and transferred onto Gel Transfer Stacks Nitrocellulose membranes (Invitrogen[®]) using the iBlot2 Dry Blotting System (Invitrogen[®]). Membranes were then incubated overnight at 4°C with the following primary antibodies: MBNL1 - MB1a(4A8) (DSHB[®], 1:1000) and MBNL2 - MB2a(3B4) (DSHB[®], 1:1000). After hybridisation of the peroxidase-conjugated secondary antibody (from 1:50000 to 1:10000), immunoreactive bands were revealed by using Amersham ECL Select Western Blotting Detection Reagents (GE Healthcare[®]). Equal protein loading was verified by the detection of β-Actin using the A3854 Monoclonal Anti-β-Actin–Peroxidase antibody (Sigma[®], 1:10000).

Electronic microscopy

Cocultures were processed in situ as previously described [30], except for a few modifications related to the use of glass instead of plastic coverslips. Following resin polymerisation, glass coverslips were dissolved with hydrofluoric acid, and plastic-embedded samples were glued on an epoxy block and cut into 70 nm ultrathin sections.

RNA-Seq library preparation and sequencing (TrueSeq polyA)

Total RNAs (control, DM1 and DKO hiPSC-derived motoneurons samples from three independent differentiations and *MBNL2*(-/-) hiPSC-derived motoneurons samples from two independent differentiations) were isolated using the RNeasy Mini extraction kit (Qiagen[®]) according to the manufacturer's protocol. RNA levels were assessed using the NanoDrop[®] technology, and quality control was evaluated by determining RNA integrity number (RIN) using the RNA screen tape technology (Agilent[®]). For each sample, 100 ng of total RNA was used. mRNAs were purified using poly-T oligo from the TruSeq Stranded kit (Illumina[®]) and were fragmented and retro-transcribed using the TruSeq Stranded kit following the protocol of the manufacturer (Illumina[®]). The final library was quantified using an Agilent High Sensitivity DNA kit before the samples were pooled in sets of six for sequencing. About 2 nM of pooled libraries were denatured, and the quantity of 1.8 pM was used for cluster generation before paired-end sequencing on an Illumina Nextseq550 (High output 2*150pb run). Samples were sequenced with an average of 89,532,366 reads (paired-end) per sample. The quality control of the sequencing data was evaluated using FastQC (v0.11.2). The reads were trimmed using Prinseq (v0.20.4) [31] (--trim-right 20) and filtered by average quality score (--trim-qual 20) and cutadapt (v1.16). Reads were mapped to Ensembl GRCh37.87 human reference using mSTAR (v2.7.3) [32]. Reads below a mapping score of 10 or multimapped were filtered using samtools (v0.1.19). The gene expression level in

each sample was quantified with HTSeq-count (v0.8.0). The differential gene expression (DEG) between conditions was calculated with DESeq2 (v1.26.0 using R v3.6.3). We consider that genes are differentially expressed when their BaseMean is greater than 20, their *p*-value adjusted is less than 0.05 and $|\log_2\text{FoldChange}|$ is upper than 0.4 (options: lfcThreshold = 0.4, altHypothesis = 'greaterAbs'). For the alternative splicing analysis, the raw reads were annotated on GRCh37.75 Ensembl reference annotation by Tophat2 (v2.0.13) and analysed using only reads on exonic junctions with FaRLINE pipeline and FasterDB database. Exons were considered differentially spliced when their adjusted *p*-value was under 0.05 and their DeltaPSI (per cent spliced-in) value was upper than 0.1. Data are available on the GEO database (GSE171988).

RT-PCR and Agilent DNA chips analysis for alternative splicing

Total RNA was extracted using the RNeasy Micro/Mini kit (Qiagen[®]) and reverse transcribed using random hexamers and Superscript III Reverse Transcriptase kit (Invitrogen[®]) according to the manufacturer's protocol. For splicing analysis, PCR amplification was carried out with recombinant Taq DNA polymerase (Invitrogen[®]) and primers listed in the supporting information Material and Method Table S3. The amplification was performed using a first step at 95°C for 3' followed by 35 cycles of 45'' at 95°C, 30'' at 60°C, 1' at 72°C and a final 10' extension at 72°C. The PCR products were analysed using Agilent[®] DNA chips and quantified with the BioAnalyzer 2100.

Statistical evaluation

All data were processed using Prism 8[®]. Values are represented as mean ± SD. Student's *t*-test was used to analyse two groups of data (**p* < 0.05; ***p* < 0.005; ****p* < 0.0005; *****p* < 0.0001). For comparisons of more than two groups, statistical analyses were performed with ordinary one-way analysis of variance (ANOVA) using Tukey's multiple comparisons test. Values of *p* < 0.05 were considered significant (**p* < 0.05; ***p* < 0.005; ****p* < 0.0005; *****p* < 0.0001). For the statistical analysis of the proportional repartition of AChR clusters by size, a two-way ANOVA using Tukey's multiple comparisons test as two independent variables (the number and the size) needed to be compared with the control condition (***p* < 0.01; ****p* < 0.001).

RESULTS

Depletion of MBNL1 and MBNL2 proteins affects neurogenesis in DM1 hiPSC-derived spinal MNs

We previously demonstrated that human embryonic stem cells carrying the causal mutation of DM1 (DM1_hESC) differentiated into motoneuronal cultures harboured nuclear foci and neuritic outgrowth

abnormalities [33]. However, the protocol of differentiation used for this previous study was inefficient with only 30% of the cells generated being spinal motoneurons and a high proportion of contaminating nonrelevant cells that hampered efforts towards pathology modelling. To circumvent this limitation, we based our approach on our recent protocol (Figure 1A) allowing the specification of hiPSCs into a population containing more than 70% spinal motoneurons [22]. This protocol was applied to differentiate hiPSC lines that we recently

developed which include independent DM1 hiPSC lines derived from three different patients (Figure 1A and supporting information Figure S1A) [24]. These lines carry a mutant *DMPK* gene that contains within the 3' UTR region approximately 2500 CTG triplet repeats. There was no major difference in terms of repeat length between donor skin fibroblasts and hiPSC lines. In addition, we generated unaffected control hiPSC, as well as one isogenic DM1 hiPSC line in which the 2700 CTG expansion had been completely excised by CRISPR/

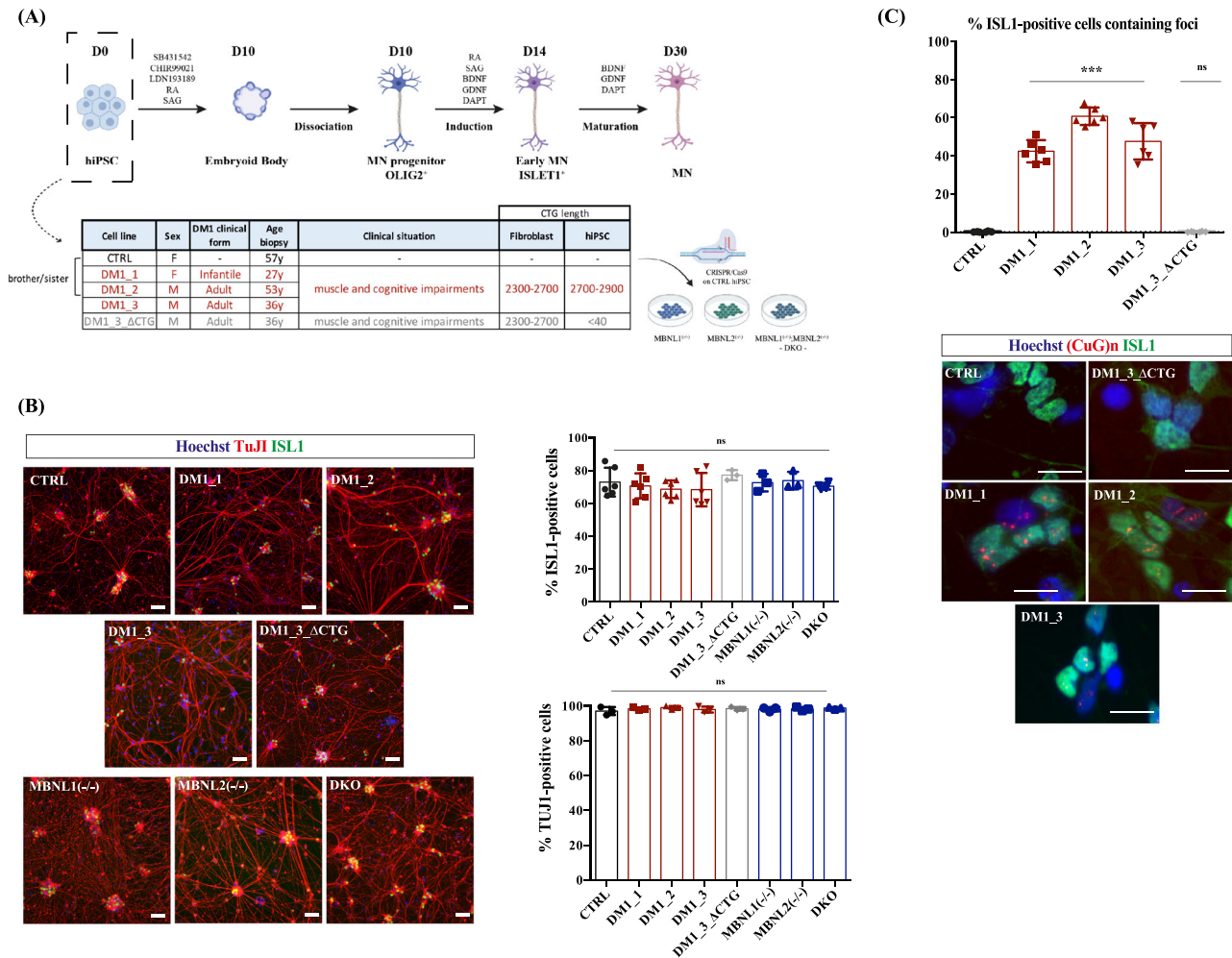


FIGURE 1 Myotonic dystrophy type I (DM1) human-induced pluripotent stem cell (hiPSC)-derived motoneurons (MNs) reproduce the main features associated with DM1. (A) Schematic representation of the differentiation protocol to convert hiPSC into MNs (created with BioRender.com) for the different hiPSC lines listed in the table below. This summary table recapitulates the sex, the age of each patient, their main clinical features and associated MDRS (muscular disability rating scale) at the time the skin fibroblast biopsies were performed. Fibroblasts from three DM1 patients and one healthy donor subject (control [CTRL]; sibling of DM1_2 patient) were used. The CTG length determined by southern blot analysis in fibroblasts and hiPSC is indicated. On the right, a schematic representation of the generation of muscleblind protein (MBNL) knock-out hiPSC cell lines. (B) Representative images of immunostaining for motoneuronal markers in hiPSC-derived MNs after 30 days of differentiation. MNs were identified by Islet1 (ISL1; Green) and TuJ1 (red) immunostaining. Nuclei were revealed by Hoechst staining (blue). Scale bar 10 μ m. On the right, the quantification of the percentage of ISL1 and TuJ1 and TuJ1-positive hiPSC-derived MNs. Data represent the mean \pm SD values from at least three independent experiments in technical triplicate. Data were analysed with an ordinary one-way analysis of variance (ANOVA), Tukey's multiple comparisons test compared with CTRL (ns: not significant). (C) Representative images of mutant *DMPK* mRNA foci (red) detected by mRNA fluorescence in situ hybridisation combined with immunolabelling for ISL1 (green) in CTRL, DM1 and DM1_3_ΔCTG-depleted hiPSC-derived MNs after 30 days of differentiation. Nuclei were detected by Hoechst staining (blue). Scale bar 10 μ m. The graph on the left represents the quantification of the percentage of ISL1-positive cells containing foci. Data represent the mean \pm SD values from at least three independent experiments in technical triplicate and were analysed with an ordinary one-way ANOVA, Tukey's multiple comparisons test compared with CTRL (****: $p \leq 0.0001$, ns: not significant).

Cas9 technology (DM1_3_ΔCTG) (Figure 1A and supporting information Figure S1B). Finally, because of the role of the two isoforms MBNL1 and MBNL2 in the muscular pathogenicity of DM1, we sought to investigate the contribution of these isoforms to motoneuron development and function by taking advantage of different hiPSC

lines we recently generated in which the genes coding these proteins had been depleted using CRISPR/Cas9 technology (Figure 1A) [24].

We determined the efficiency of the differentiation by quantifying the percentage of cells expressing the generic motoneuron marker ISL1 as well as the pan-neuronal marker TUJ1 over the total of cells

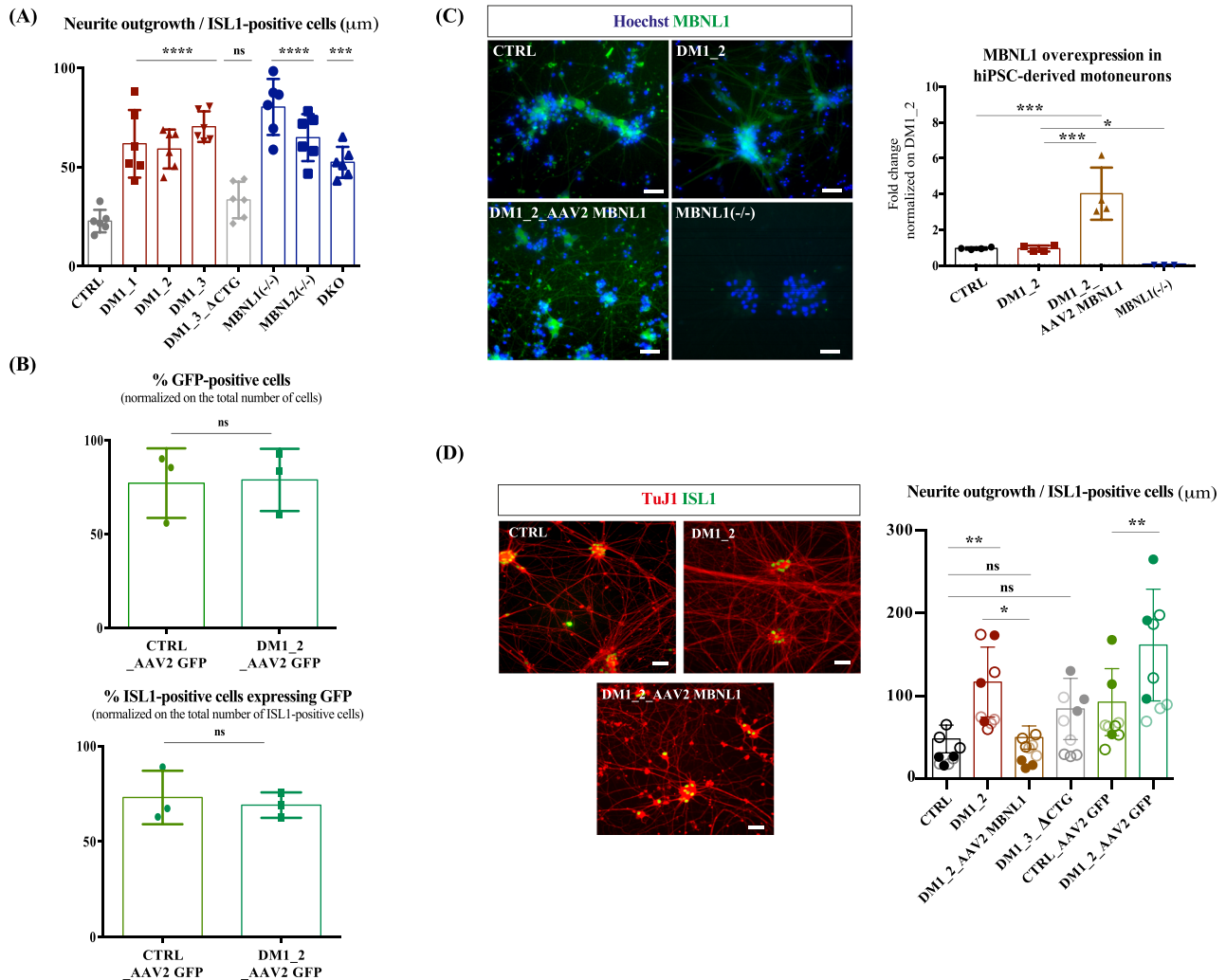


FIGURE 2 Muscleblind protein (MBNL)-dependent abnormal neuritic outgrowth in myotonic dystrophy type I (DM1) human-induced pluripotent stem cell (hiPSC)-derived MNs. (A) Quantification of neurite length (μm) per hiPSC-derived motoneuron (MN) at day 30 of differentiation by co-immunostaining for TuJ1 and Islet1 (ISL1). Data are represented as the mean ± SD values from at least four independent experiments in technical triplicate and were analysed with an ordinary one-way analysis of variance (ANOVA), Tukey's multiple comparisons test compared with control (CTRL) (***: $p \leq 0.001$, ****: $p \leq 0.0001$, ns: not significant). (B) Percentage of GFP-positive cells and ISL1-positive cells expressing GFP following pAAV2[Exp]-EF1A>EGFP:WPRES transduction of hiPSC-derived MNs (at day 30). Data represent the mean ± SD values from three independent experiments in three technical triplicates and were analysed with Student's t-test (ns: not significant). (C) Representative images of MBNL1 immunostaining (green, nuclei in blue) in CTRL, DM1, MBNL1 knock-out and DM1 hiPSC-derived MNs transduced by pAAV2 [Exp]-EF1A>hMBNL1[NM_021038.5]:WPRES. Scale bar 10 μm. MBNL1 overexpression was determined by the quantification of immunofluorescence in hiPSC-derived MNs 20 days posttransduction with pAAV2[Exp]-EF1A>hMBNL1[NM_021038.5]:WPRES. Data were normalised on the values generated for mock-transduced DM1_2. Data are represented as the mean ± SD values from three independent experiments in technical triplicate and were analysed with an ordinary one-way ANOVA, Tukey's multiple comparisons test compared with DM1_2 (***: $p \leq 0.001$, *: $p < 0.05$). (D) Representative images of colabelling for ISL1 (green) and TuJ1 (red) in CTRL, DM1 and MBNL1 transduced hiPSC-derived MNs. Scale bar 10 μm. Quantification of the neuritic outgrowth (μm) per hiPSC-derived MNs transduced by pAAV2[Exp]-EF1A>hMBNL1[NM_021038.5]:WPRES was determined at day 30 of differentiation. Data represent the mean ± SD values from three independent experiments in technical triplicate (highlighted with nuanced colours) and were analysed with an ordinary one-way ANOVA, Tukey's multiple comparisons test compared with CTRL and DM1_2 (*: $p < 0.05$, **: $P < 0.005$, ns: not significant).

determined by Hoechst staining. More than 95% of cells were neurons (determined by the expression of the pan-neuronal Class III tubulin marker, TUJ1), independently of the cell line. As previously described [27], around 70% of the cells were motoneurons regardless of the cell line demonstrating that the specification into MNs was not affected by the DM1 mutation (Figure 1B and supporting information Figure S2). Mutant RNA aggregates were detected in 40% to 60% of DM1 hiPSC-derived MNs, while none were observed in the control and isogenic DM1_3_ΔCTG hiPSC-derived MNs (Figure 1C). We also confirmed the specific lack of expression of the MBNL paralogs at the protein level in the different gene-edited hiPSC lines differentiated into MNs (supporting information Figure S3A–C).

As previously described, increased neuritic outgrowth was specifically observed in DM1 hiPSC-derived MNs compared with control and DM1_3_ΔCTG hiPSC-derived MNs (Figure 2A). Quantification of the neuritic length revealed a significantly increased neuritic outgrowth in *MBNL1*^(-/-), *MBNL2*^(-/-) and *MBNL1*^{(-/-); MBNL2}^(-/-) (DKO) hiPSC-derived MNs as observed in DM1-derived MNs (Figure 2A). To confirm the relationship between the loss of MBNL expression and neuritic defects, we evaluated the possibility of reversing the neuritic phenotype by overexpressing MBNL proteins in DM1 cells. In view of the profile expression of MBNL proteins during the differentiation of hiPSC into spinal motoneurons, we overexpressed MBNL1 by using an AAV2 vector at day 10 of the protocol of differentiation (progenitor stage) as the peak expression of this protein is observed at this time point (supporting information Figure S3A,B). As a control and to evaluate the efficiency of transduction, cells were also transduced with an AAV2 expressing GFP. As expected from previous work [28], approximately 70% of hiPSC-derived MNs expressed GFP and MBNL1 overexpression was confirmed (Figure 2B,C). The quantitative analysis of the neuritic outgrowth revealed that overexpressing MBNL1 in DM1 hiPSC-derived motoneurons led to a normalisation of excessive neuritogenesis observed in the DM1 condition (Figure 2D).

A 96-well plate coculture to study the communication between human skeletal muscle cells and hiPSC-derived motoneurons

We next sought to investigate whether this abnormal development of MNs may affect their communication with their skeletal muscle targets. For this purpose, we developed in vitro cocultures derived from hiPSC-derived MNs and primary human skeletal muscle cells (supporting information Figure S4A) using micropatterned 96-well plates. In these plates, each well contains around 100 micropatterns that were shown to favour the formation of aligned and striated mature myofibers from human primary skeletal muscle cells [23]. The use of a 96-well plate format also offers the possibility to analyse in parallel a large number of conditions (Figure 3A). To evaluate the maturity and functionality of this coculture system, we first characterised cocultures generated with healthy cells. Thus, motoneurons derived from hiPSC from a healthy donor were seeded on top of human primary

skeletal muscle cells derived from a healthy control (Figure 3B). The morphology of the cocultures was followed by a time-lapse phase contrast microscopy tracking the development of neurite arborisation and the fusion of skeletal muscle cells (supporting information Figure S4B,C; see Movie S1). Immunostaining for ISL1 confirmed appropriate maturation of hiPSC-derived motoneurons (ISL1) (Figure 3C) and mature myotubes was revealed by the expression of Myosin II Heavy Chain (MHC) (Figure 3D). The presence of hiPSC-derived MNs did not affect the myotube area (Figure 3D), although a significant increase in postsynaptic AChR clustering was detected in their presence when compared with myotubes alone (Figure 3E and supporting information Figure S4D). The detection and localisation of different presynaptic markers such as synaptophysin, the vesicular acetylcholine transporter and bassoon, in close proximity to AChR clusters confirmed the existence of synapse formation (Figure 4A and supporting information Figure S4D). These observations were validated by transmission electron microscopy revealing close contacts between skeletal muscle cells and hiPSC-derived motoneurons. The presence of presynaptic vesicles as well as apposed electron-dense zones suggested the presence of AChR clusters at junctional zones (Figure 4B).

In terms of functionality, muscular contractions were observed 4 days after the addition of hiPSC-derived MNs. Quantification of twitching activities revealed a significant effect of hiPSC-derived MNs on the capacity of human primary skeletal muscle cells to contract (supporting information Figure S5A; see Movie S2). Another important functional parameter consisted of the measurement of the capacity of hiPSC-derived MNs to induce Ca²⁺ transients in skeletal muscle cells. Extensive characterisation of this parameter was performed under different conditions. We first demonstrated that the addition of hiPSC-derived MNs led to a significant increase in Ca²⁺ transients when compared with human primary skeletal muscle cells alone (Figure 4C and supporting information Figure S5B; see Movies S3 and S4). The specificity of these Ca²⁺ transients was evaluated using pharmacological approaches. Application of the neurotransmitter glutamate to activate motoneurons triggered a significant increase in the Ca²⁺ signal peaks (supporting information Figure S5C; see Movie S5). In contrast, the excitation of skeletal muscle cells was totally abolished by d-tubocurarine, a competitive inhibitor of AChR, indicating that the Ca²⁺ oscillations were mediated by AChR clusters (supporting information Figure S5D; see Movie S6). Finally, treatment with Botulinum neurotoxin Type-A (BoNT/A), known to induce a prolonged blockage of neurotransmitter release from the nerve terminal in vivo and in hiPSC-based neuronal models [34, 35], led to a significant reduction of Ca²⁺ activity confirming that the Ca²⁺ oscillations observed in skeletal muscle cells were dependent on neurotransmitter release by hiPSC-derived MNs (Figure 4D).

These functional analyses indicate that the micropatterned cocultures at this stage (day 7) recapitulate key phenotypical and functional features of early neuromuscular junction development and therefore offer new perspectives to study impairment of this intercellular structure in diseases.

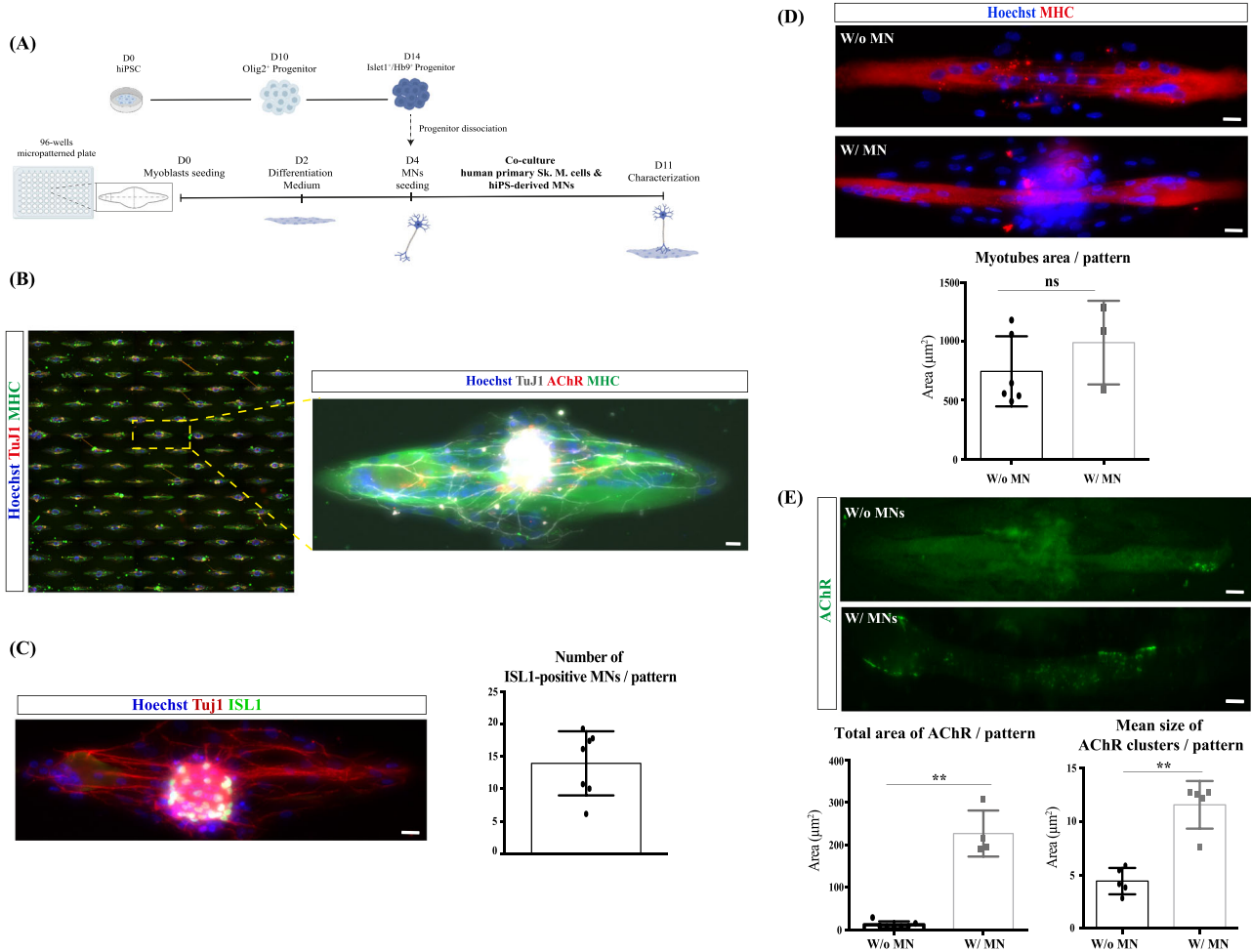


FIGURE 3 Human-induced pluripotent stem cell (hiPSC)-derived motoneurons (MNs) enhance acetylcholine receptor (AChR) clustering after 7 days of coculture. (A) Schematic representation of the protocol developed for the coculture between hiPSC-derived MNs and human skeletal muscle cells. MNs differentiated from hiPSC for 14 days were dissociated and plated on top of human primary skeletal muscle cells differentiated for 2 days. Cocultures were kept at least for 7 days. (B) Representative images of an entire well from a 96-well plate immunostained for myosin heavy chain (MF20, green) and TuJ1 (red). Nuclei were detected by Hoechst staining (blue). Each well contains about 100 micropatterns. Scale bar: 100 µm. On the right, a higher magnification of one micropattern stained for TuJ1 (Grey), acetylcholine receptors (AChR, red) and myosin heavy chain (MF20, Green). Nuclei were detected by Hoechst (blue). Scale Bar 10 µm. (C) Representative images of hiPSC-derived MNs stained for ISL1 (Green), and TuJ1 (red). Nuclei were detected by Hoechst staining (blue). Scale bar 10 µm. On the right, quantification of the mean number of hiPSC-derived MNs per pattern determined by ISL1 positive cells. Data represent the mean ± SD values from 7 independent experiments in technical triplicate (at least 100 micropatterns/condition/experiment). (D) Representative images of skeletal muscle cells immunolabelled using myosin heavy chain marker (MHC) with (w/) or without (w/o) hiPSC-derived MNs. On the right, quantification of myotube area (µm²) per pattern with (w/) or without (w/o) hiPSC-derived MNs. Data are presented as the mean ± SD values from at least three independent experiments in technical triplicate (at least 100 micropatterns/experiment/condition) and were analysed with Student's t-test (ns: Not significant). (E) Representative images of immunolabelling for acetylcholine receptors clusters (AChR, Green). Scale Bar 10 µm. On the right, the quantification of the total area and the mean size of AChR clusters (µm²) per pattern as described in the supporting information method. Data are presented as the mean ± SD values from at least three independent experiments in technical triplicate (at least 100 micropatterns/condition/experiment) and were analysed with Student's t-test (**: $p < 0.005$).

Impaired communication of DM1 and MBNL-depleted hiPSC-derived spinal MNs with skeletal muscle targets

To evaluate the capacity of DM1 and MBNL-depleted hiPSC-derived MNs to interact with skeletal muscle cells properly and functionally, we employed a hybrid system in which wild-type control primary skeletal muscle cells were cocultured with DM1 or MBNL-depleted

hiPSC-derived MNs (Figure 5A). Firstly, no difference was detected in the number of hiPSC-derived MNs (Figure 5B or supporting information Figure S6A) or in the myogenic area (Figure 5C) As previously observed in the monocultures of DM1 and MBNL-depleted hiPSC-derived MNs, there was a defect in a neurite outgrowth (Figure 5D). This result was also confirmed by quantifying the number of neuritic branches per micropattern (Figure 5E). This quantification revealed an

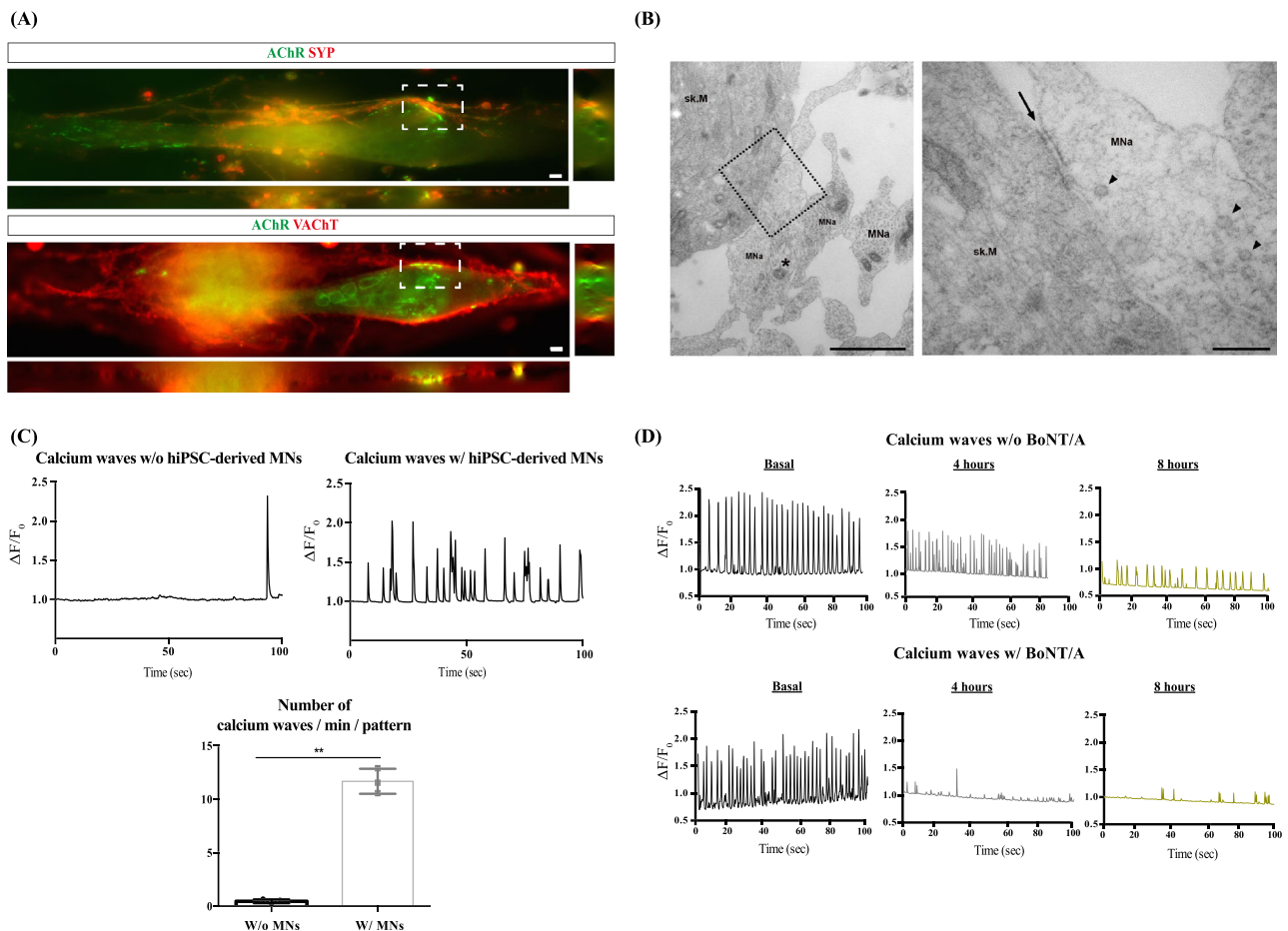


FIGURE 4 Immunofluorescence and ultrastructural studies reveal contacts between presynaptic and postsynaptic compartments confirmed by functional analyses. (A) Co-immunostaining for acetylcholine receptor (AChR) and different synaptic vesicle markers: synaptophysin (SYP) and vesicular acetylcholine transporter (VACHT). Orthogonal views are represented from different planes (x/z, y/z). Scale bar: 10 μ m. (B) Transmission electron micrographs of a contact between a hiPSC-derived motoneuron (MNa) axon (obliquely cut microtubules indicated by the asterisk) and a skeletal muscle cell. Scale bar = 1 μ m. The dotted square is enlarged in the right micrograph, where black arrowheads indicate synaptic vesicles in the presynaptic zone and the arrow points to plasmalemmal electron densities on both sides of the contact. Scale bar = 200 nm. (C) Representative diagram of calcium waves recorded for 100 s with (w/) or without (w/o) human-induced pluripotent stem cell (hiPSC)-derived MNs. $\Delta F/F_0$ representation after background correction. On the right, the quantification of the number of calcium waves per minute and per pattern in the absence or presence of hiPSC-derived MNs. Data are presented as the mean \pm SD values from three independent experiments in technical triplicate (at least 100 micropatterns/condition/experiment) and were analysed with Student's *t*-test (**: $p < 0.005$). (D) Graphical representation of calcium waves recorded in basal condition or 4 and 8 h after the addition of a solution of 5 nM botulinum neurotoxin type-A (BoNT/A). $\Delta F/F_0$ representation after background correction.

increased number of neurite branches in DM1 and MBNL-depleted conditions when compared with control or CTG-depleted DM1 hiPSC lines. In parallel to the neuritic phenotypes, quantitative analysis of the mean size of AChR clusters revealed impaired endplate maturation in DM1 and MBNL-depleted hiPSC-derived MNs as compared with control or isogenic control DM1 (Figure 5F). The size distribution of AChR clusters revealed that the total area of AChR was not affected, but that there was a higher proportion of small AChR clusters in DM1 and MBNL-depleted hiPSC-derived MNs when compared with controls (Control and DM1_3_ΔCTG) (Figure 5F and supporting information Figure S6B,C).

To evaluate the functional consequences of these phenotypes, Ca^{2+} oscillations induced by hiPSC-derived MNs were measured in

healthy skeletal muscle cells. A significant increase in the frequency of calcium transients was observed in the presence of DM1 and MBNL-depleted hiPSC-derived MNs (Figure 6A,B and supporting information Figure S7; see movies S7–S12). In contrast, no difference was observed between Control and DM1_3_ΔCTG depleted cocultures (Figure 6A,B). Because the muscular component of the cocultures consisted of healthy control skeletal muscle cells, we concluded that the abnormal behaviour of the myofibers could be attributed to DM1 and MBNL-depleted hiPSC-derived spinal MNs. Our data strongly suggest that, under pathological conditions, spinal MNs may contribute anterogradely to the NMJ defects observed in DM1. Thus, the increased number of smaller clusters of AChR in DM1 and MBNL-depleted hiPSC-derived MNs might explain the increase in calcium transients.

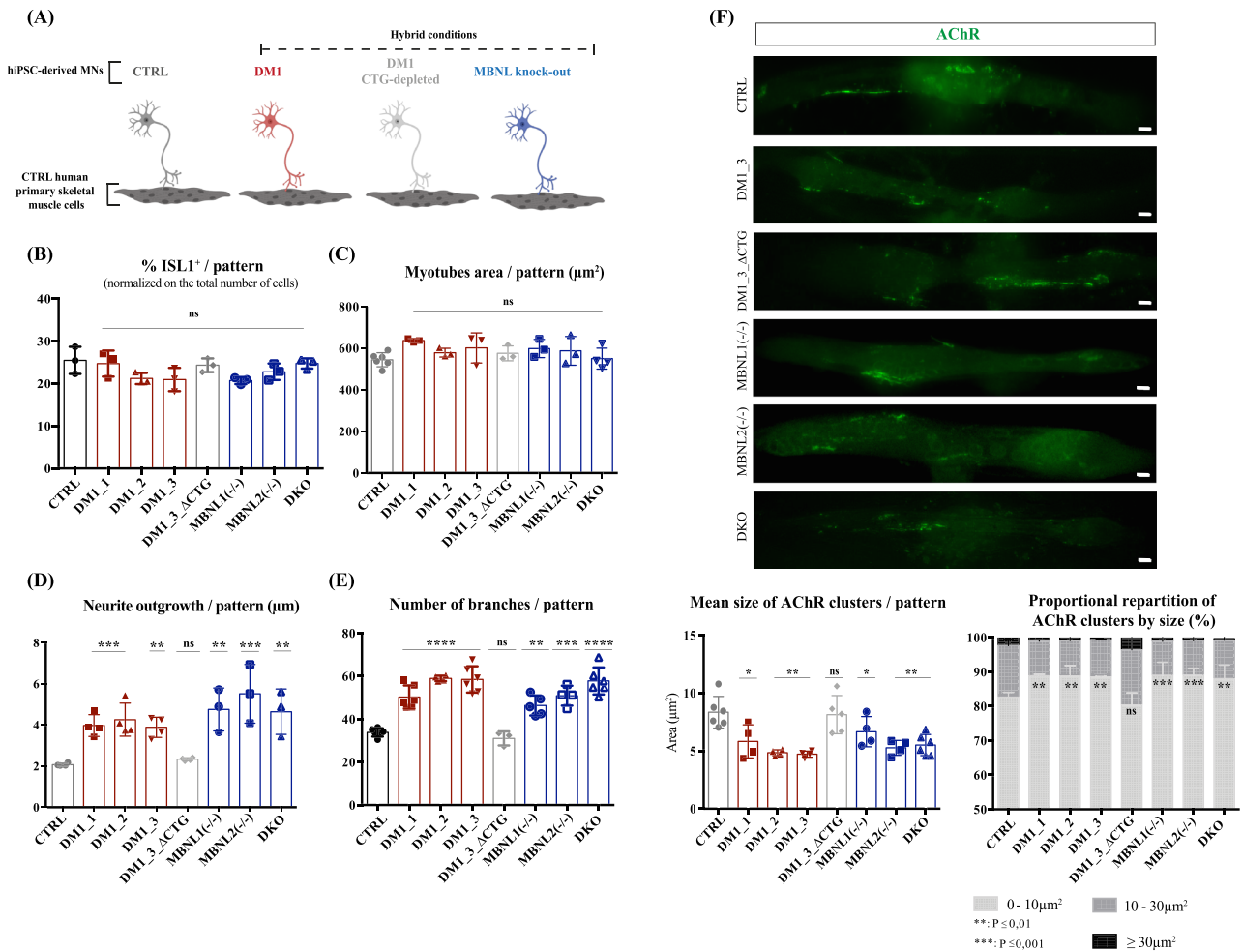


FIGURE 5 Synaptic defects observe at prelevel and postlevel in myotonic dystrophy type I (DM1) and muscleblind protein (MBNL) depleted coculture hybrid conditions. (A) Schematic representation of hybrid coculture systems (*created with BioRender.com*). (B) Percentage of Islet1 (ISL1) -positive cells per pattern after 7 days of coculture. (C) Quantification of myotube area per pattern (μm²) after 7 days of coculture. (D) Quantification of neurite length (μm) per pattern after 7 days of coculture. (E) Quantification of the number of neurite branches of human-induced pluripotent stem cell (hiPSC)-derived motoneurons (MNs) in different hybrid coculture systems. For all the quantifications, data are represented as the mean ±SD values from at least three independent experiments in technical triplicate (at least 150 micropatterns per condition and per experiment were analysed). Data were analysed with an ordinary one-way analysis of variance (ANOVA), Tukey’s multiple comparisons test compared with control (CTRL), (**: $P \leq 0.01$, ***: $P \leq 0.001$, ****: $P \leq 0.0001$, ns: not significant). (F) Representative acetylcholine receptor (AChR) immunolabelling (Green) images in cocultures for 7 days with MNs derived from the different hiPSC lines. Scale bar: 10 μm. On the top right, quantification of the mean size of AChR clusters per pattern (μm²) as represented as the mean ± SD values from at least three independent experiments in technical triplicate (at least 50 micropatterns/condition/experiment). Data were analysed with an ordinary one-way ANOVA, Tukey’s multiple comparisons test compared with CTRL (*: $P \leq 0.05$, **: $P \leq 0.01$, ns: not significant). On the bottom right, the histogram represented the proportional repartition (%) of AChR clusters by size (0–10 μm², 10–30 μm², 30 μm² and more) in different hybrid coculture systems. Data are presented as the mean ± SD values from at least three independent experiments in technical triplicate (at least 50 micropatterns/condition/experiment). Data were analysed with a two-way ANOVA, Tukey’s multiple comparisons test compared with CTRL (**: $P \leq 0.01$, ***: $P \leq 0.001$, ns: not significant).

Misregulation of common synaptic pathways in DM1 and MBNL-depleted hiPSC-derived motoneurons

We previously identified in DM1 hES-derived motoneuronal cultures defective expression of the *SLITRK2* gene that has been implicated in nerve fibre growth and thus may be correlated to the neuritic phenotype [33]. Consistent with our previous results, we confirmed *SLITRK2* misexpression in DM1 hiPSC-derived motoneurons as well as its

normalisation in CTG-depleted DM1 hiPSC-derived motoneurons. Strikingly, the misexpression of *SLITRK2* was not observed in the absence of MBNL proteins, suggesting the involvement of additional molecular MBNL-dependent mechanisms in the synaptic defects observed (supporting information Figure S8A).

To further investigate these molecular mechanisms, we conducted comparative transcriptomic analyses between DM1, MBNL-depleted and control hiPSC-derived motoneurons where #1, #2 and

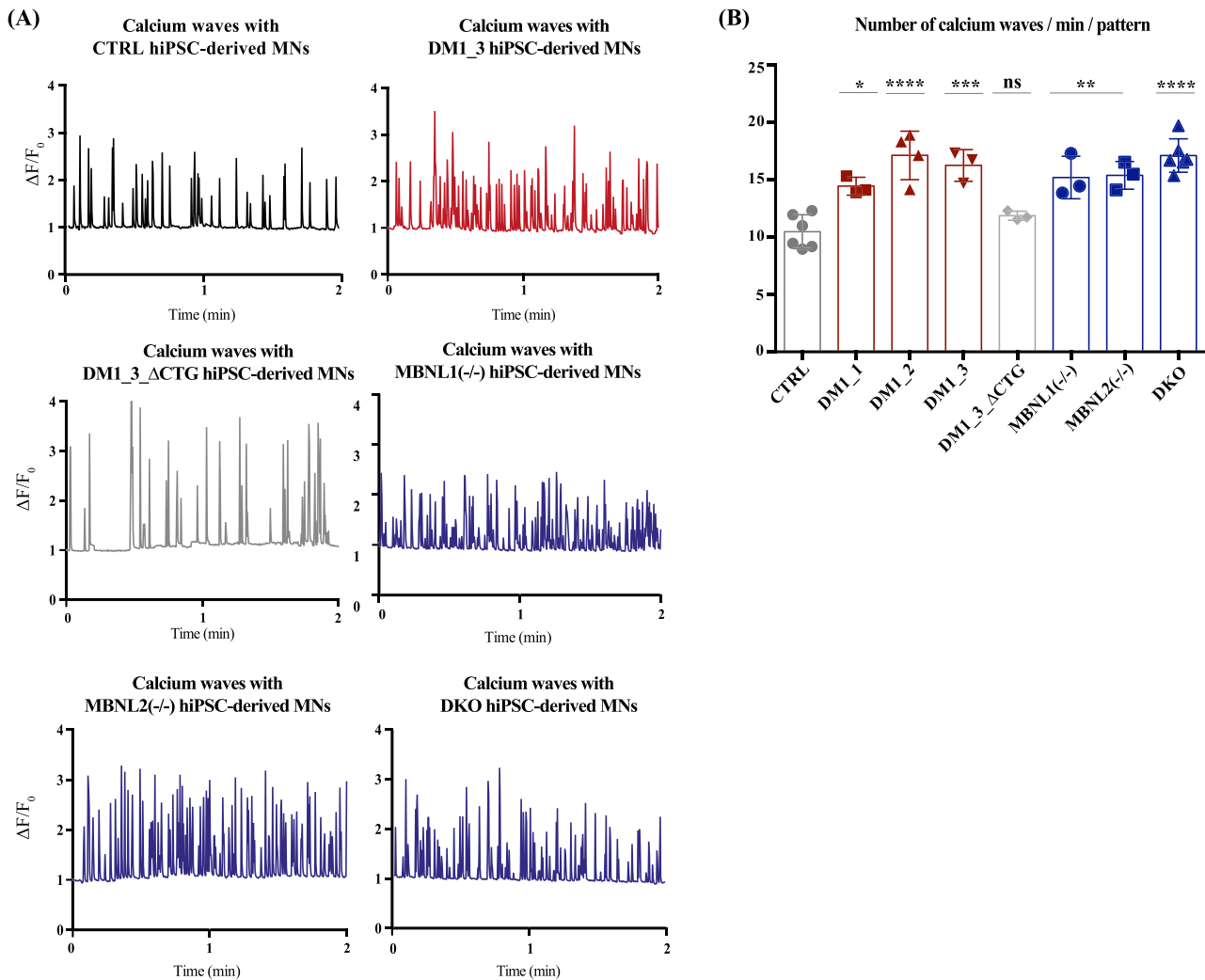


FIGURE 6 Communication defect between hiPSC-derived motoneurons (MNs) and skeletal muscle cells in myotonic dystrophy type I (DM1) and muscleblind protein (MBNL)-depleted conditions. (A) Representative diagrams of calcium waves (time = 2 min) recorded in human primary skeletal muscle cells in different hybrid conditions (CTRL -control- in dark grey, DM1 in burgundy, DM1_3_ΔCTG in light grey and MBNL knockout conditions in blue). $\Delta F/F_0$ representation is indicated after background correction. (B) Quantification of the number of calcium waves recorded in human primary skeletal muscle cells per pattern and per min after 7 days of coculture. Data are presented as the mean \pm SD values from at least three independent experiments in technical triplicate (at least 100 micropatterns/condition/experiment) and were analysed with an ordinary one-way analysis of variance (ANOVA), Tukey's multiple comparisons test compared with CTRL (*: $P \leq 0.05$, **: $P \leq 0.01$, ***: $P \leq 0.001$, ****: $P \leq 0.0001$, ns: not significant).

#3 correspond to three independent differentiations. Distinct transcriptomic profiles between these three conditions were validated by the principal component analysis (PCA) and heatmap representation (Figure 7A and supporting information Figure S8B). The comparison between DM1 and control hiPSC-derived motoneurons led to the identification of 328 genes differentially expressed in DM1 compared with control motoneurons (Figure 7B and Table S4). A more pronounced difference was observed between DKO and control hiPSC-derived motoneurons with a total of 723 differentially expressed genes (DEGs) (Figure 7B and Table S4). Gene ontology analysis of DEGs in DM1 vs control hiPSC-derived motoneurons revealed enrichment in pathways related to 'anterograde trans-synaptic signalling', 'chemical synaptic transmission' and more generally 'nervous system

development' (supporting information Figure S8C). Strikingly, most of these synaptic-related biological processes were also found to be downregulated in DM1 hiPSC-derived motoneurons (Figure 7C). Similar observations were found in DKO hiPSC-derived motoneurons compared with the control (Figure 7D and supporting information Figure S8D). Among the 328 DEGs observed in DM1 hiPSC-derived motoneurons, 137 (42%) were also misregulated in DKO hiPSC-derived motoneurons (Figure 7E). Even though these common DEGs may not be considered direct proof of MBNL's role in these dysregulations, they highlight some pathways in which MBNL might be involved either directly or indirectly. Interestingly, functional annotation of common DEGs also revealed that the most relevant GO terms concerned 'nervous system development', 'anterograde

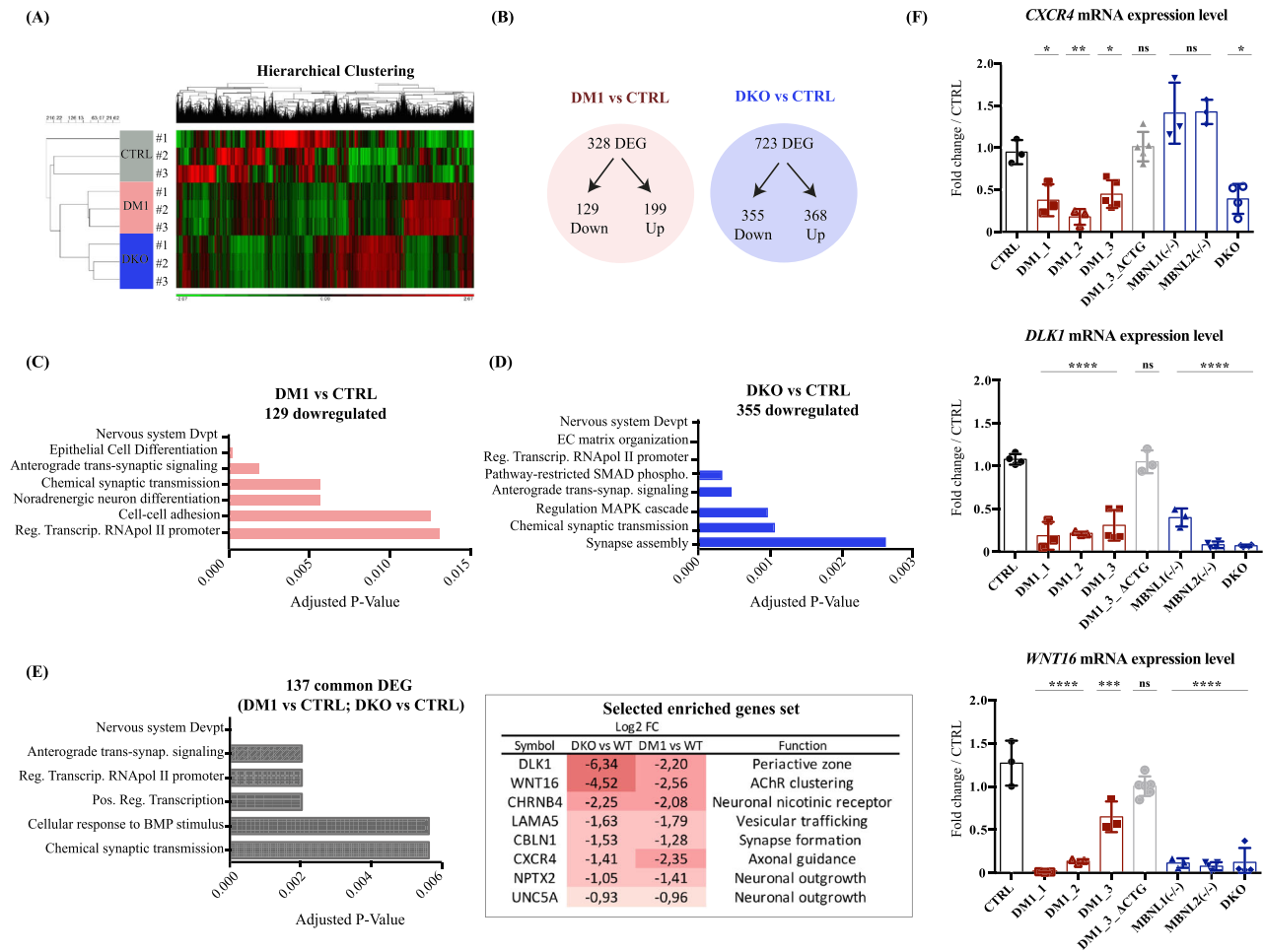


FIGURE 7 Myotonic dystrophy type I (DM1) mutation and muscleblind protein (MBNL) depletion affect the expression of genes related to synaptic functions. (A) Hierarchical clustering of differentially expressed genes (DEG) detected in DM1 and DKO human-induced pluripotent stem cell (hiPSC)-derived motoneurons (MNs) compared with control (CTRL) hiPSC-derived MNs. Gene expression is represented by a colour code ranging from green for underexpressed genes to red for overexpressed genes. (B) Schematic representation of the number of DEG in DM1 (red) and DKO (Green) hiPSC-derived MNs. (C) Genes set enrichment analysis using EnrichR on the 129 downregulated genes in DM1 hiPSC-derived MNs when compared with CTRL hiPSC-derived MNs (EnrichR analysis using GO Biological process 2018 database). (D) Genes set enrichment analysis using EnrichR on the 355 downregulated genes in DKO hiPSC-derived MNs when compared with CTRL hiPSC-derived MNs (EnrichR analysis using GO Biological process 2018 database). (E) Genes set enrichment analysis using EnrichR on the 137 common deregulated genes between DM1 vs CTRL hiPSC-derived MNs and DKO vs CTRL hiPSC-derived MNs conditions (EnrichR analysis using GO Biological process 2018 database). On the right, a list of specific deregulated genes in the panel of 137 genes commonly identified between DM1 vs CTRL hiPSC-derived MNs and DKO vs CTRL hiPSC-derived MNs conditions. (F) Quantification by RT-qPCR of *CXCR4*, *DLK1* and *WNT16* mRNA expression level in hiPSC-derived MNs after normalisation with *Cyclophilin A*, *18S* and *GAPDH* levels. Data are presented as the mean ± SD values from three independent experiments in technical triplicate and were analysed with an ordinary one-way analysis of variance (ANOVA), Tukey's multiple comparisons test compared with CTRL (**: $P \leq 0.01$, ***: $P \leq 0.001$, ****: $P \leq 0.0001$, ns: not significant).

trans-synaptic signalling' and 'chemical synaptic transmission' (Figure 7E). Several of these misregulated genes caught our attention due to their function in NMJ development (Figure 7E and supporting information Figure S8E). Among them, we specifically confirmed the misexpression of *CXCR4*, *DLK1* and *WNT16* which all have been associated with NMJ development in animal models (Figure 7F) [36–39].

Due to the important role played by MBNL proteins in the regulation of alternative splicing, we pursued our analysis by evaluating the differentially spliced exons (DSEs). Functional annotations of these

DSEs (Table S5) revealed several genes also related to synapse structure and function (Figure 8A,B). Among the 236 DSE observed in DM1 hiPSC-derived motoneurons, only 48 DSE (20%) were found common to the DKO condition (Figure 8C) suggesting that additional MBNL-independent mechanisms might be involved in the alternative splicing defects observed in DM1. Functional annotation analysis of the common transcriptomic data revealed that the most relevant GO terms concerned neuronal outgrowth such as 'axogenesis' or 'axon guidance' (Figure 8C). As an example, we confirmed the missplicing of *CAST* and *COL13A1*, two genes previously shown to be respectively

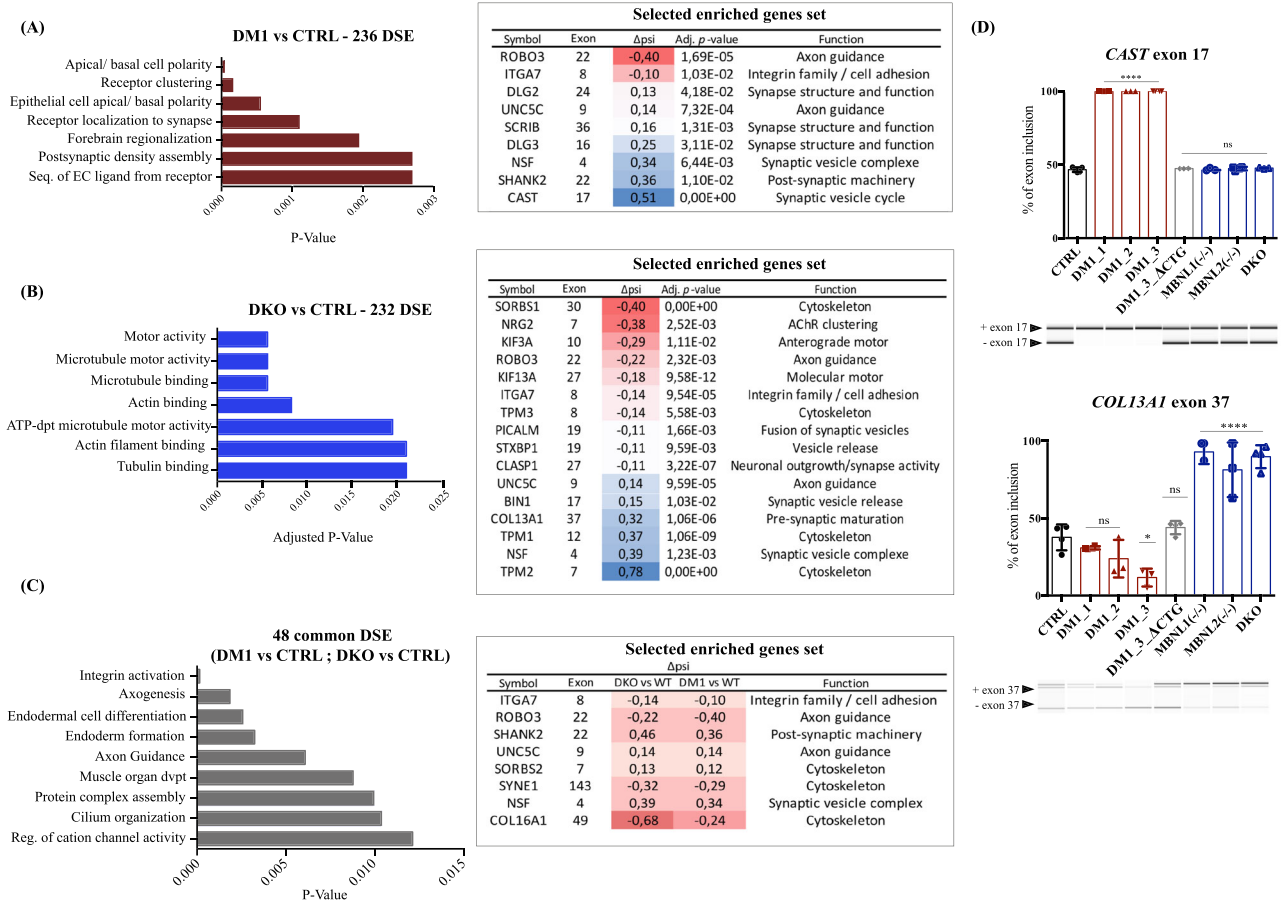


FIGURE 8 Myotonic dystrophy type I (DM1) mutation and loss of muscleblind protein (MBNL1) and MBNL2 proteins lead to a large number of alternative splicing defects related to molecular motor activity and synaptic functions. (A) Genes set enrichment analysis using EnrichR on the 236 differentially spliced exons (DSE) in DM1 hiPSC-derived motoneurons (MNs) when compared with CTRL hiPSC-derived MNs (EnrichR analysis using GO Biological process 2018 database). The table on the right provides a list of specific genes differentially spliced-in DM1 hiPSC-derived MNs. (B) Genes set enrichment analysis using EnrichR on the 232 differentially spliced exons (DSE) in DKO hiPSC-derived MNs when compared with CTRL hiPSC-derived MNs (EnrichR analysis using GO Molecular Function 2018 database). The table on the right provides a list of specific genes differentially spliced-in DKO hiPSC-derived MNs. (C) Genes set enrichment analysis using EnrichR on the 48 common differentially spliced exons (DSE) between DM1 vs CTRL hiPSC-derived MNs and DKO vs CTRL hiPSC-derived MNs conditions (EnrichR analysis using GO Biological process 2018 database). On the right, list of specific misspliced genes in the panel of genes commonly identified between DM1 vs CTRL hiPSC-derived MNs and DKO vs CTRL hiPSC-derived MNs conditions. (D) Alternative splicing analysis for *CAST* exon 17 and *COL13A1* exon 37 in hiPSC-derived MNs. Data represent the mean \pm SD values from three independent experiments in technical triplicate and were analysed with an ordinary one-way analysis of variance (ANOVA), Tukey's multiple comparisons test compared with CTRL (***: $P \leq 0.001$, ****: $P \leq 0.0001$, ns: not significant).

involved in the organisation of presynaptic active zones [40] and in motor endplate maturation [41] (Figure 8D).

As Mbnl2 was shown to be an important splicing factor involved in brain development [42], we evaluated the consequences of its loss on gene expression defects. Interestingly, among the 200 DEG in *MBNL2*($-/-$) hiPSC-derived motoneurons (supporting information Figure S9A), 123 genes (61.5%) were common to DKO hiPSC-derived motoneurons (supporting information Figure S9B). As observed in DKO and DM1 conditions, the enriched pathways deregulated in the absence of MBNL2 concerned the nervous system and synaptic functions (supporting information Figure S9A,B). The gene ontology analysis of the 236 misspliced events observed in the *MBNL2*($-/-$) hiPSC-derived MNs (supporting information Figure S9C) showed that

pathways involved in protein localisation and actin cytoskeleton were enriched. However, only 30% of common missplicing events were observed in *MBNL2*($-/-$) and DKO conditions, suggesting a significant role of MBNL1 in these defects (supporting information Figure S9D).

DISCUSSION

The main findings of the present study are the anterograde neuronal contribution of spinal MNs to the NMJ defects observed in Myotonic Dystrophy type 1 and that this contribution is dependent on MBNL proteins.

Assigning a precise correspondence between our *in vitro* findings and the disease development in DM1 patients is difficult and remains, at this point, speculative. It is striking however that abnormal morphological motor nerve terminals, including expanded terminal arborisations and multiple endplates on the same muscle fibre, were observed in DM1 patients' biopsies [15, 16, 43, 44]. More recently, neurophysiological studies in two different cohorts of DM1 patients reported neuromuscular transmission abnormalities [17, 18]. One of the most striking observations has been the consistent detection of mutant mRNA aggregates in the nuclei of spinal motoneurons in DM1 patients [45]. Altogether, this has raised a question concerning the contribution of motoneurons in neuromuscular defects in DM1.

Along those lines, our group has previously demonstrated the potential of using human pluripotent stem cells carrying the causal mutation of DM1 (DM1_hPSC) to confirm the presence of nuclear foci and neuritic outgrowth abnormalities within DM1_hPSC derived motoneuronal cultures [33]. Recent advances in human pluripotent stem cell biology have fuelled the prospect of generating cell types that are difficult, even impossible, to access in patients. Whereas the first protocols for motoneuron differentiation were long and inefficient, tremendous progress has been made in the ability to manipulate these cells and a growing number of protocols are now based only on the use of small molecules or morphogens [46]. Here, we demonstrated that the protocol we generated a couple of years ago [17] is suitable for disease modelling and more specifically for highlighting disease-specific synaptic defects. This is in line with several recent studies that used this protocol for a broader spectrum of neuromuscular diseases such as ALS or SMA [47–51] or for screening the effect of neurotoxins [28].

At the mechanistic level, we had previously identified in DM1 hES-derived motoneuronal cultures the defective expression of the *SLITRK2* gene that might be correlated to the neuritic phenotype [33]. Consistent with these results, we confirmed the downregulated expression of *SLITRK2* in DM1 hiPSC-derived motoneurons as well as its normalisation in CTG-depleted DM1 hiPSC-derived motoneurons. Nonetheless, this *SLITRK2* dysregulated expression is not observed in the absence of MBNL proteins, suggesting the involvement of additional MBNL-dependent mechanisms in the synaptic defects observed. Our results reveal similar phenotypes in DM1 and MBNL-depleted hiPSC-derived motoneurons. Thus, the relationship between abundant neuritogenesis and reduced synaptogenesis may reflect an MBNL-dependent alteration in recognition signals between the two synapse partners. Consistent with our observations, immature NMJs with fragmented AChR clusters were previously described in *Mbnl1*^(-/-); *Mbnl2*^(+/-) mice [52]. Similarly, *Caenorhabditis elegans* Muscleblind homologue *mb-1* was shown to be required for the proper formation of neuromuscular synapses [53]. Surprisingly, NMJ defects of *mb-1* mutant can be rescued by neuronal expression but not by muscle expression of *mb-1*, suggesting that MBL-1 functions in neurons regulate synapse formation. Whereas the major pathological features of the DM1 brain have been previously shown to be associated with the disruption of the MBNL2-mediated developmental splicing programme [42], deletion of MBNL1 or MBNL2 led to the

same synaptic defect at the neuromuscular level. We can therefore hypothesise that both paralogs might account for neuromuscular defects. These results raised the question of how and by which mechanisms MBNL proteins might be involved in the development of neuromuscular interactions.

At the molecular level, the comparative transcriptomic analyses between DM1 and MBNL-depleted hiPSC-derived MNs revealed the deregulation of several pathways related to anterograde trans-synaptic signalling and cytoskeletal elements of axonal transport. Interestingly, these results are concordant with previous transcriptomic analyses performed in the hippocampi of *Mbnl2*^(-/-) mice [54]. Due to the large number of deregulated genes, we identified, the hypothesis of a unique gene underlying the different phenotypes is unlikely and combined misexpression of several actors involved in synaptic function might be considered. MBNL proteins also have significant cytoplasmic expression and have been proposed to contribute to the regulation of mRNA stability [55–59] or localisation [58, 60]. MBNL proteins could therefore determine the localisation of mRNA through splicing, with long 3'UTR transcripts being trafficked to dendrites, while short 3'UTR are retained in the soma [61, 62]. Moreover, Wang and colleagues showed that MBNL1 could bind 3'UTR mRNA of SNAP25 and VAMP1, two synaptic proteins, to regulate their neuronal localisation [58]. MBNL proteins associated with mRNA form a messenger ribonucleoprotein (mRNP) complex itself integrated into granules allowing the transport of mRNA along axons thanks to cytoskeletal machinery [63]. These data have led to an emerging hypothesis that RNA localisation functions of MBNL are important for proper synapse function and that mislocalized RNAs might account for some neurological features associated with DM1. Interestingly, the transcriptomic analysis of hiPSC-derived MNs revealed several enriched deregulated pathways involved in the cytoskeleton machinery, molecular motor, protein localisation and organelle transport along microtubules in DM1 and MBNL-depleted conditions. It could be interesting therefore to evaluate the trafficking of synaptic vesicles along microtubules and the quantification of synaptic vesicles at the presynaptic active zone under our different hybrid conditions to assess the potential role of MBNL proteins.

Altogether, our results suggest that DM1 might not be only considered a muscle-specific disease but also a disease of motoneurons. Therefore, we suggest that MNs could also be considered targets for future therapy for this fatal neuromuscular disease. Consequently, the involvement of MNs in neuromuscular junction defects in DM1 might deserve further attention and investigation. Our approach to modelling human neuromuscular communication should pave the way for the study of a greater number of neuromuscular diseases. However, the development of an NMJ model in which both neuron and muscle components are derived from the same individual is of great interest for modelling diseases of genetic aetiology. The recent description of a 3D model of the neuromuscular junction from human pluripotent stem cells should open new perspectives to circumvent the challenge of fully recapitulating the neuromuscular system [64, 65]. The emergence of these new models, together with complex and specialised basal laminas, should also permit the integration of other cell types

such as the terminal Schwann cells important for the development and maintenance of the neuromuscular system.

ACKNOWLEDGEMENTS

I-STEM is part of the Biotherapies Institute for Rare Diseases (BIRD) supported by the Association Française contre les Myopathies (AFM-Téléthon). This project was supported by grants from Laboratoire d'Excellence Revive (Investissement d'Avenir; ANR-10-LABX-73), the Region Ile-de-France via the doctoral school « Innovation Thérapeutique, du fondamental à l'appliqué » (ED 569) from Paris Saclay University and Agence Nationale de la Recherche (ANR). We thank Lina El-Kassar and Karine Giraud-Triboulet for karyotyping the cell lines, the bioproduction platform for the large-scale production of control myoblasts. We also thank Florine Roussange for her help at the revision step. We gratefully acknowledge support from the PSMN (Pôle Scientifique de Modélisation Numérique) of the ENS of Lyon for the computing resource.

CONFLICT OF INTEREST

The authors declare no conflicts of interest.

ETHICS STATEMENT

Informed consent was obtained from all the patients included in this study, complying with the ethical guidelines of the institutions and with the legislation requirements. Experimental protocols were approved by the French Minister of Health (2019-A02599-48).

AUTHOR CONTRIBUTIONS

J.T.B., C.L., L.S. and C.M.: conception and design. J.T.B. and C.M.: investigation and data collection. J.T.B., C.L., J.P., H. P, M.J. A.C. and C.M.: formal analysis and interpretation. J.L.: electronic microscopy. J.D.D.L and C.N.: Neurotoxin experiment. A.M., A.G. and M.G.-P.: Engineered cell lines. D.F. and C.M.: provision of different cellular resources. C.M., L.S. and C.L.: financial support. J.T.B. and C.M.: manuscript writing.

PEER REVIEW

The peer review history for this article is available at <https://publons.com/publon/10.1111/nan.12876>.

DATA AVAILABILITY STATEMENT

The data that support the findings of this study are openly available in GEO (<https://www.ncbi.nlm.nih.gov/geo/query/acc.cgi?acc=GSE171988>), reference number GSE171988.

ORCID

Cécile Martinat  <https://orcid.org/0000-0002-5234-1064>

REFERENCES

1. Brook JD, McCurrach ME, Harley HG, et al. Molecular basis of myotonic dystrophy: expansion of a trinucleotide (CTG) repeat at the 3' end of a transcript encoding a protein kinase family member. *Cell*. 1992;69(2):385-808. doi:10.1016/0092-8674(92)90154-5
2. Mahadevan M, Tsilfidis C, Sabourin L, et al. Myotonic dystrophy mutation: an unstable CTG repeat in the 3' untranslated region of the gene. *Science*. 1992;255(5049):1253-1255. doi:10.1126/science.1546325
3. Johnson NE, Butterfield RJ, Mayne K, et al. Population-based prevalence of myotonic dystrophy type 1 using genetic analysis of state-wide blood screening program. *Neurology*. 2021;96(7):e1045-e1053. doi:10.1212/WNL.0000000000011425
4. Lopez-Morato M, Brook JD, Wojciechowska M. Small molecules which improve pathogenesis of myotonic dystrophy type 1. *Front Neurol*. 2018;9:349. doi:10.3389/fneur.2018.00349
5. Thornton CA, Wang E, Carrell EM. Myotonic dystrophy: approach to therapy. *Curr Opin Genet Dev*. 2017;44:135-140. doi:10.1016/j.gde.2017.03.007
6. Echenne B, Bassez G. Congenital and infantile myotonic dystrophy. *Handb Clin Neurol*. 2013;113:1387-1393. doi:10.1016/B978-0-444-59565-2.00009-5
7. Harper PS. *Myotonic dystrophy*. Vol. 37. Thirded; 2001.
8. Ho TH, Charlet BN, Poulos MG, Singh G, Swanson MS, Cooper TA. Muscleblind proteins regulate alternative splicing. *EMBO j*. 2004;23(15):3103-3112. doi:10.1038/sj.emboj.7600300
9. Fardaei M, Rogers MT, Thorpe HM, et al. Three proteins, MBNL, MBLL and MBXL, co-localize in vivo with nuclear foci of expanded-repeat transcripts in DM1 and DM2 cells. *Hum Mol Genet*. 2002;11(7):805-814. doi:10.1093/hmg/11.7.805
10. Miller JW, Urbinati CR, Teng-Umuay P, et al. Recruitment of human muscleblind proteins to (CUG)(n) expansions associated with myotonic dystrophy. *EMBO j*. 2000;19(17):4439-4448. doi:10.1093/emboj/19.17.4439
11. Nakamori M, Sobczak K, Puwanant A, et al. Splicing biomarkers of disease severity in myotonic dystrophy. *Ann Neurol*. 2013;74(6):862-872. doi:10.1002/ana.23992
12. Charlet BN, Savkur RS, Singh G, Phillips AV, Grice EA, Cooper TA. Loss of the muscle-specific chloride channel in type 1 myotonic dystrophy due to misregulated alternative splicing. *Mol Cell*. 2002;10(1):45-53. doi:10.1016/S1097-2765(02)00572-5
13. Mankodi A, Takahashi MP, Jiang H, et al. Expanded CUG repeats trigger aberrant splicing of CIC-1 chloride channel pre-mRNA and hyperexcitability of skeletal muscle in myotonic dystrophy. *Mol Cell*. 2002;10(1):35-44. doi:10.1016/S1097-2765(02)00563-4
14. Kanadia RN, Shin J, Yuan Y, et al. Reversal of RNA missplicing and myotonia after muscleblind overexpression in a mouse poly (CUG) model for myotonic dystrophy. *Proc Natl Acad Sci U S A*. 2006;103(31):11748-11753. doi:10.1073/pnas.0604970103
15. Allen DE, Johnson AG, Woolf AL. The intramuscular nerve endings in dystrophia myotonica—a biopsy study by vital staining and electron microscopy. *J Anat*. 1969;105(Pt 1):1-26.
16. Coers C, Telerman-Toppet N, Gerard JM. Terminal innervation ratio in neuromuscular disease. II. Disorders of lower motor neuron, peripheral nerve, and muscle. *Arch Neurol*. 1973;29(4):215-222. doi:10.1001/archneur.1973.00490280027003
17. Bombelli F, Lispi L, Porrini SC, et al. Neuromuscular transmission abnormalities in myotonic dystrophy type 1: a neurophysiological study. *Clin Neurol Neurosurg*. 2016;150:84-88. doi:10.1016/j.clineuro.2016.08.020
18. Krishnan AV, Kiernan MC. Axonal function and activity-dependent excitability changes in myotonic dystrophy. *Muscle Nerve*. 2006;33(5):627-636. doi:10.1002/mus.20516
19. Panaite PA, Gantelet E, Kraftsik R, Gourdon G, Kuntzer T, Barakat-Walter I. Myotonic dystrophy transgenic mice exhibit pathologic abnormalities in diaphragm neuromuscular junctions and phrenic nerves. *J Neuropathol Exp Neurol*. 2008;67(8):763-772. doi:10.1097/NEN.0b013e318180ec64
20. Wheeler TM, Thornton CA. Myotonic dystrophy: RNA-mediated muscle disease. *Curr Opin Neurol*. 2007;20(5):572-576. doi:10.1097/WCO.0b013e3282ef6064

21. Barbeau S, Tahraoui-Bories J, Legay C, Martinat C. Building neuromuscular junctions in vitro. *Development*. 2020;147(22). doi:10.1242/dev.193920
22. Maury Y, Come J, Piskowski RA, et al. Combinatorial analysis of developmental cues efficiently converts human pluripotent stem cells into multiple neuronal subtypes. *Nat Biotechnol*. 2015;33(1):89-96. doi:10.1038/nbt.3049
23. Young J, Margaron Y, Fernandes M, et al. MyoScreen, a high-throughput phenotypic screening platform enabling muscle drug discovery. *SLAS Discovery: Advancing Life Sciences R & D*. 2018;23(8):790-806. doi:10.1177/2472555218761102
24. Merien A, Tahraoui-Bories J, Cailleret M, et al. CRISPR gene editing in pluripotent stem cells reveals the function of MBNL proteins during human in vitro myogenesis. *Hum Mol Genet*. 2021;31(1):41-56. doi:10.1093/hmg/ddab218
25. Lo Scudato M, Poulard K, Sourd C, et al. Genome editing of expanded CTG repeats within the human DMPK gene reduces nuclear RNA foci in the muscle of DM1 mice. *Mol Ther*. 2019;27(8):1372-1388. doi:10.1016/j.yjthe.2019.05.021
26. Maury Y, Poydenot P, Brinon B, et al. Pluripotent stem cell-based drug screening reveals cardiac glycosides as modulators of myotonic dystrophy type 1. *iScience*. 2019;11:258-271. doi:10.1016/j.isci.2018.12.019
27. Maury Y, Côme J, Piskowski RA, et al. Combinatorial analysis of developmental cues efficiently converts human pluripotent stem cells into multiple neuronal subtypes. *Nat Biotechnol*. 2015;33(1):89-96. doi:10.1038/nbt.3049
28. de Lamotte JD, Polentes J, Roussange F, et al. Optogenetically controlled human functional motor endplate for testing botulinum neurotoxins. *Stem Cell Research & Therapy*. 2021;12(1):599. doi:10.1186/s13287-021-02665-3
29. Lamotte JD, Roqueviere S, Gautier H, et al. hiPSC-derived neurons provide a robust and physiologically relevant in vitro platform to test botulinum neurotoxins. *Front Pharmacol*. 2020;11:617867. doi:10.3389/fphar.2020.617867
30. Laine J, Skoglund G, Fournier E, Tabti N. Development of the excitation-contraction coupling machinery and its relation to myofibrillogenesis in human iPSC-derived skeletal myocytes. *Skeletal Muscle*. 2018;8(1):1. doi:10.1186/s13395-017-0147-5
31. Schmieder R, Edwards R. Quality control and preprocessing of meta-genomic datasets. *Bioinformatics*. 2011;27(6):863-864. doi:10.1093/bioinformatics/btr026
32. Dobin A, Davis CA, Schlesinger F, et al. STAR: ultrafast universal RNA-seq aligner. *Bioinformatics*. 2013;29(1):15-21. doi:10.1093/bioinformatics/bts635
33. Marteyn A, Maury Y, Gauthier MM, et al. Mutant human embryonic stem cells reveal neurite and synapse formation defects in type 1 myotonic dystrophy. *Cell Stem Cell*. 2011;8(4):434-444. doi:10.1016/j.stem.2011.02.004
34. Elliott M, Favre-Guilmond C, Liu SM, et al. Engineered botulinum neurotoxin B with improved binding to human receptors has enhanced efficacy in preclinical models. *Sci Adv*. 2019;5(1):eaau7196. doi:10.1126/sciadv.aau7196
35. Duchesne De Lamotte J, Polentes J, Lesueur L, et al. Optogenetically controlled human functional motor endplate for testing botulinum neurotoxins. *Submitted*. 2021.
36. Nakata K, Abrams B, Grill B, et al. Regulation of a DLK-1 and p38 MAP kinase pathway by the ubiquitin ligase RPM-1 is required for presynaptic development. *Cell*. 2005;120(3):407-420. doi:10.1016/j.cell.2004.12.017
37. Kurup N, Yan D, Goncharov A, Jin Y. Dynamic microtubules drive circuit rewiring in the absence of neurite remodeling. *Curr Biol*. 2015;25(12):1594-1605. doi:10.1016/j.cub.2015.04.061
38. Lieberam I, Agalliu D, Nagasawa T, Ericson J, Jessell TM. A Cxcl12-CXCR4 chemokine signaling pathway defines the initial trajectory of mammalian motor axons. *Neuron*. 2005;47(5):667-679. doi:10.1016/j.neuron.2005.08.011
39. Zhang B, Liang C, Bates R, Yin Y, Xiong WC, Mei L. Wnt proteins regulate acetylcholine receptor clustering in muscle cells. *Mol Brain*. 2012;5(1):7. doi:10.1186/1756-6606-5-7
40. Ohtsuka T. CAST: functional scaffold for the integrity of the presynaptic active zone. *Neurosci Res*. 2013;76(1-2):10-15. doi:10.1016/j.neures.2013.03.003
41. Haronen H, Zainul Z, Naumenko N, et al. Correct expression and localization of collagen XIII are crucial for the normal formation and function of the neuromuscular system. *Eur J Neurosci*. 2019;49(11):1491-1511. doi:10.1111/ejn.14346
42. Charizanis K, Lee KY, Batra R, et al. Muscleblind-like 2-mediated alternative splicing in the developing brain and dysregulation in myotonic dystrophy. *Neuron*. 2012;75(3):437-450. doi:10.1016/j.neuron.2012.05.029
43. Macdermot V. The histology of the neuromuscular junction in dystrophonia myotonica. *Brain*. 1961;84(1):75-84. doi:10.1093/brain/84.1.75
44. Borg J, Edstrom L, Butler-Browne GS, Thornell LE. Muscle fibre type composition, motoneuron firing properties, axonal conduction velocity and refractory period for foot extensor motor units in dystrophonia myotonica. *J Neurol Neurosurg Psychiatry*. 1987;50(8):1036-1044. doi:10.1136/jnnp.50.8.1036
45. Wheeler TM, Krym MC, Thornton CA. Ribonuclear foci at the neuromuscular junction in myotonic dystrophy type 1. *Neuromuscul Disord*. 2007;17(3):242-247. doi:10.1016/j.nmd.2006.12.015
46. Giacomelli E, Vahsen BF, Calder EL, et al. Human stem cell models of neurodegeneration: from basic science of amyotrophic lateral sclerosis to clinical translation. *Cell Stem Cell*. 2022;29(1):11-35. doi:10.1016/j.stem.2021.12.008
47. Dafinca R, Barbagallo P, Farrimond L, et al. Impairment of mitochondrial calcium buffering links mutations in C9ORF72 and TARDBP in iPSC-derived motor neurons from patients with ALS/FTD. *Stem Cell Reports*. 2020;14(5):892-908. doi:10.1016/j.stemcr.2020.03.023
48. Mehta AR, Gregory JM, Dando O, et al. Mitochondrial bioenergetic deficits in C9orf72 amyotrophic lateral sclerosis motor neurons cause dysfunctional axonal homeostasis. *Acta Neuropathol*. 2021;141(2):257-279. doi:10.1007/s00401-020-02252-5
49. Selvaraj BT, Livesey MR, Zhao C, et al. C9ORF72 repeat expansion causes vulnerability of motor neurons to Ca²⁺-permeable AMPA receptor-mediated excitotoxicity. *Nat Commun*. 2018;9(1):347. doi:10.1038/s41467-017-02729-0
50. Ma XR, Prudencio M, Koike Y, et al. TDP-43 represses cryptic exon inclusion in the FTD-ALS gene UNC13A. *Nature*. 2022;603(7899):124-130. doi:10.1038/s41586-022-04424-7
51. Hensel N, Cieri F, Santonicola P, et al. Impairment of the neurotrophic signaling hub B-Raf contributes to motoneuron degeneration in spinal muscular atrophy. *Proc Natl Acad Sci U S A*. 2021;118(18). doi:10.1073/pnas.2007785118
52. Lee KY, Li M, Manchanda M, et al. Compound loss of muscleblind-like function in myotonic dystrophy. *EMBO Mol Med*. 2013;5(12):1887-1900. doi:10.1002/emmm.201303275
53. Spilker KA, Wang GJ, Tugizova MS, Shen K. Caenorhabditis elegans muscleblind homolog mbl-1 functions in neurons to regulate synapse formation. *Neural Dev*. 2012;7(1):7. doi:10.1186/1749-8104-7-7
54. Goodwin M, Mohan A, Batra R, et al. MBNL sequestration by toxic RNAs and RNA misprocessing in the myotonic dystrophy brain. *Cell Rep*. 2015;12(7):1159-1168. doi:10.1016/j.celrep.2015.07.029
55. Du H, Cline MS, Osborne RJ, et al. Aberrant alternative splicing and extracellular matrix gene expression in mouse models of myotonic dystrophy. *Nat Struct Mol Biol*. 2010;17(2):187-193. doi:10.1038/nsmb.1720
56. Osborne RJ, Lin X, Welle S, et al. Transcriptional and post-transcriptional impact of toxic RNA in myotonic dystrophy. *Hum Mol Genet*. 2009;18(8):1471-1481. doi:10.1093/hmg/ddp058

57. Wang ET, Ward AJ, Cherone JM, et al. Antagonistic regulation of mRNA expression and splicing by CELF and MBNL proteins. *Genome Res.* 2015;25(6):858-871. doi:[10.1101/gr.184390.114](https://doi.org/10.1101/gr.184390.114)
58. Wang ET, Cody NA, Jog S, et al. Transcriptome-wide regulation of pre-mRNA splicing and mRNA localization by muscleblind proteins. *Cell.* 2012;150(4):710-724. doi:[10.1016/j.cell.2012.06.041](https://doi.org/10.1016/j.cell.2012.06.041)
59. Masuda A, Andersen HS, Doktor TK, et al. CUGBP1 and MBNL1 preferentially bind to 3' UTRs and facilitate mRNA decay. *Sci Rep.* 2012;2(1):209. doi:[10.1038/srep00209](https://doi.org/10.1038/srep00209)
60. Adereth Y, Dammai V, Kose N, Li R, Hsu T. RNA-dependent integrin alpha3 protein localization regulated by the muscleblind-like protein MLP1. *Nat Cell Biol.* 2005;7(12):1240-1247. doi:[10.1038/ncb1335](https://doi.org/10.1038/ncb1335)
61. An JJ, Gharami K, Liao GY, et al. Distinct role of long 3' UTR BDNF mRNA in spine morphology and synaptic plasticity in hippocampal neurons. *Cell.* 2008;134(1):175-187. doi:[10.1016/j.cell.2008.05.045](https://doi.org/10.1016/j.cell.2008.05.045)
62. Shigeoka T, Jung H, Jung J, et al. Dynamic axonal translation in developing and mature visual circuits. *Cell.* 2016;166(1):181-192. doi:[10.1016/j.cell.2016.05.029](https://doi.org/10.1016/j.cell.2016.05.029)
63. Van Driesche SJ, Martin KC. New frontiers in RNA transport and local translation in neurons. *Dev Neurobiol.* 2018;78(3):331-339. doi:[10.1002/dneu.22574](https://doi.org/10.1002/dneu.22574)
64. Afshar Bakooshli M, Lippmann ES, Mulcahy B, et al. A 3D culture model of innervated human skeletal muscle enables studies of the adult neuromuscular junction. *Elife.* 2019;8:8. doi:[10.7554/eLife.44530](https://doi.org/10.7554/eLife.44530)
65. Faustino NA, Cooper TA. Pre-mRNA splicing and human disease. *Genes Dev.* 2003;17(4):419-437. doi:[10.1101/gad.1048803](https://doi.org/10.1101/gad.1048803)

SUPPORTING INFORMATION

Additional supporting information can be found online in the Supporting Information section at the end of this article.

How to cite this article: Tahraoui-Bories J, Mérien A, González-Barriga A, et al. MBNL-dependent impaired development within the neuromuscular system in myotonic dystrophy type 1. *Neuropathol Appl Neurobiol.* 2023;49(1):e12876. doi:[10.1111/nan.12876](https://doi.org/10.1111/nan.12876)